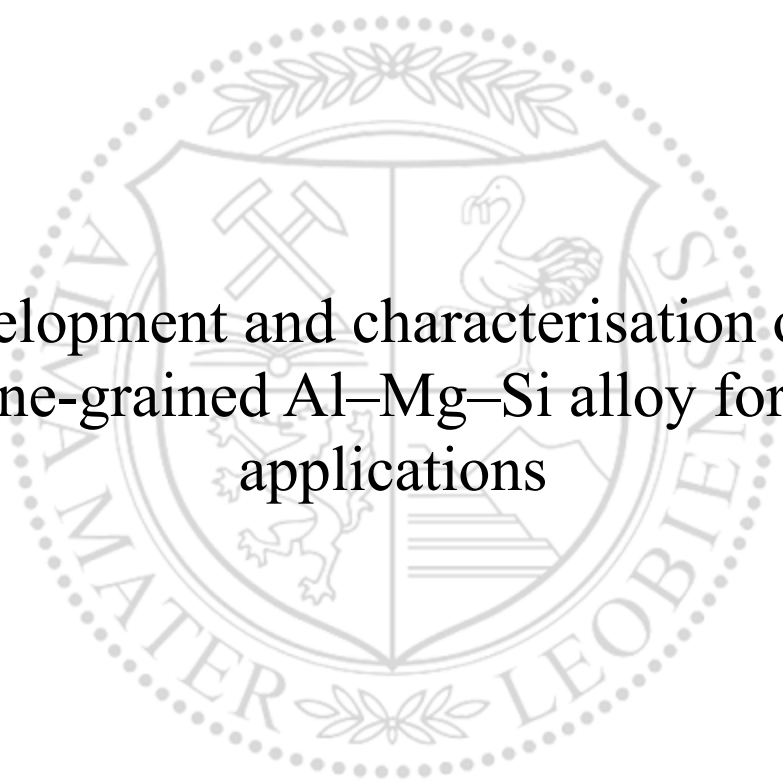




Chair of Nonferrous Metallurgy

Master's Thesis



Development and characterisation of an
ultrafine-grained Al–Mg–Si alloy for space
applications

Sandra Veronica Gonzaga Hernandez

August 2024



MONTANUNIVERSITÄT LEOBEN

www.unileoben.ac.at

AFFIDAVIT

I declare on oath that I wrote this thesis independently, did not use any sources and aids other than those specified, have fully and truthfully reported the use of generative methods and models of artificial intelligence, and did not otherwise use any other unauthorized aids.

I declare that I have read, understood and complied with the "Good Scientific Practice" of the Montanuniversität Leoben.

Furthermore, I declare that the electronic and printed versions of the submitted thesis are identical in form and content.

Date 26.08.2024

A handwritten signature in blue ink, appearing to read 'S. Gonzaga'.

Signature Author

Sandra Veronica Gonzaga Hernandez

Acknowledgements

First of all, I would like to thank my family, especially my parents, Lazaro Gonzaga and Veronica Hernandez, for giving me all the necessary means to get to where I am today, for all the support they have given me before and during my studies. I owe all this to you both.

I want to express my gratitude to everyone who contributed to the completion of my Master thesis with their support. The greatest thanks go to my mentor at the Chair of Non-ferrous Metallurgy, Ass.-Prof. Matheus A. Tunes for providing the topic of this master's thesis, the discussions, and all the support during the revisions and corrections of my work. Without his cooperation, my work would certainly not have been completed in a timely fashion.

I also would like to say thank you very much for both Uni.-Prof. Dipl.-Ing. Dr. mont. Stefan Pogastcher and Vice-Rector Uni-Prof. Dipl.-Ing. Dr. mont. Helmut Antrekowitsch for funding, infrastructure and support of my thesis work.

Very special thanks to Dipl.-Ing. Patrick Willenshofer who gave me excellent support, advice, corrections and always was open to help with my questions and problems. I would also like to thank Dipl.-Ing. Dr. mont. Thomas Kremmer who supported me with training for the use and interpretation of TEM analysis. I would also like to thank miss Nadine Tatzreiter for the help and tips with the metallographic sample preparation and for the training of various devices at the chair.

I would also like to thank to my AMASE friends in Leoben for your support during my master thesis and for being a great example, especially to David Marin, Manuela Marcos, Alan Arceta and Carmen Herrero.

Contents

Affidavit	I
Acknowledgements	II
List of Figures	V
List of Tables	VII
Acronyms	VIII
Abstract	1
Kurzfassung	2
1 Introduction	4
2 Literature review	7
2.1 Space materials and the choice of aluminium	7
2.1.1 Requirements for space materials	7
2.1.2 Challenges for aluminium in space	8
2.1.3 Brief overview of the irradiation effects in aluminium alloys	9
2.1.4 The advent of radiation-resistant aluminium alloys	10
2.2 Ultrafine-grained aluminium alloys	11
2.2.1 The principle of severe plastic deformation	11
2.2.2 High-pressure torsion	13
2.2.3 The thermal stability challenge for UFG aluminium alloys	14
2.3 The Al–Mg–Si system and the AA6061 alloy	14
2.3.1 Coarse grained AA6061	18
2.3.2 Ultrafine-grained AA6061	20
2.4 Objectives of this work	21
3 Methodology	22
3.1 Description of the experimental methods	22
3.1.1 Arc/spark optical emission spectrometry	22
3.1.2 Differential scanning calorimetry	22
3.1.3 Transmission electron microscopy	23
3.1.4 Scanning transmission electron microscopy	24

3.1.5	<i>In situ</i> TEM experiments	25
3.2	Synthesis and characterisation of the UFG AA6061 alloy	26
3.2.1	Preparation of the CG AA6061 alloy	26
3.2.2	Synthesis of the UFG AA6061 alloy	27
3.2.3	Thermal analysis	27
3.2.4	Electron-microscopy measurements	28
3.2.5	<i>In situ</i> TEM thermal stability measurements	28
3.2.6	Grain size estimation	29
4	Results	30
4.1	The coarse grained AA6061 alloy	30
4.1.1	Grain size measurements	30
4.1.2	Differential Scanning Calorimetry	31
4.1.3	Conventional and analytical scanning/transmission electron microscopy	32
4.1.4	The estimation of the Mg/Si ratio	33
4.2	The ultrafine-grained Al–Mg–Si alloy	35
4.2.1	Differential Scanning Calorimetry	35
4.2.2	Conventional and analytical scanning/transmission electron microscopy	35
4.2.3	The estimation of the Mg/Si ratio	38
4.2.4	Grain size measurements	39
4.2.5	<i>In situ</i> TEM heating	39
5	Discussion	41
5.1	Comparison CG vs UFG alloy	41
5.1.1	Coarse grained alloy	41
5.1.2	Ultra-fine grained alloy	43
5.1.3	Remarks on the differences between the heat-treated CG and UFG AA6061 alloys	44
5.2	<i>In situ</i> thermal stability of the UFG AA6061 alloy	45
6	Conclusions	47
	Bibliography	49
	Appendix	57

List of Figures

1	The NASA's space shuttle program used aluminium and its alloys in several forms spread all over the design and fuselage of the multiple spacecrafts [12]. Note: Reproduced from work performed by the U.S. Government, public use permitted.	5
2	T-phase precipitates were observed to survive to irradiation doses around 1 dpa. In the figure, the survivability of the T-phase was attested by monitoring its diffraction signal in the alloy's diffraction pattern as a function of the irradiation dose. Note: Reproduced from the open access paper by Tunes <i>et al.</i> [2].	10
3	Graphical representation of SPD techniques. Note: Redrawn and reproduced from [43].	12
4	Schematic illustration of HPT processing. Note: The drawing was extracted from Zhilyaev <i>et al.</i> [52].	13
5	A new UFG crossover alloy made with AlMgZnCuAg was recently show to present superior thermal stability than pure UFG aluminium and some select UFG aluminium alloys made from commercial counterparts. In the figure, BFTEM micrographs show the UFG microstructure as a function of temperature where it is possible to note the action of T-phase precipitates in pinning grain boundaries. Note: Figure was reproduced from the open access paper by Willenshofer <i>et al.</i> [16]. . .	15
6	DSC and TEM characterisation data obtained by Dutta <i>et al.</i> [67] in the commercial CG AA6061 alloy. Note: Montage made with the original DSC plots, BFTEM micrographs and SAED patterns from the work of Dutta <i>et al.</i> [67]. Note: Reproduction granted by Springer Nature.	19
7	Schematic illustration of a DSC heat flux cell. The sample is denoted by S and the reference is denoted by R. Note: Reproduced from Lang <i>et al.</i> [74].	23
8	A cross-sectional profile of a common TEM. Note: Reproduced from Fultz and Howe [75].	24
9	STEM mode within the TEM. Extracted from Tunes [76].	25
10	TEM holder with an E-chip used for heating experiments with <i>in situ</i> TEM. Note: Extracted from Protochips <i>apud</i> Coradini [81].	26
11	Final shape of the CG AA6061 alloy after homogenisation, hot- and cold-rolling prior HPT.	27
12	HPT equipment for synthesis of UFG AA6061 alloy and the final shape obtained after the HPT processing.	27
13	Foils prepared with 100 μm after mechanical polishing.	28

14	HPT sample used both for electron-microscopy investigations and <i>in situ</i> TEM heating experiments.	29
15	Microstructural morphology of the CG AA6061 alloy after processing. Micrograph was obtained through OM with polarised light after etching. Average grain size was $67.6 \pm 18.9 \mu\text{m}$	30
16	The thermogram obtained via DSC from the CG AA6061 alloy. These experiments were performed with a linear heating rate of $10^\circ\text{C}\cdot\text{min}^{-1}$	31
17	S/TEM micrographs and SAED patterns obtained from the CG AA6061 alloy at different temperatures according to the identified DSC peaks in Figure 16. Note: the SAED pattern had their colour inverted and both brightness and contrast were adjusted to better visualisation of the spots pertaining to the precipitates.	32
18	The STEM-EDX mapping of CG AA6061 alloy samples show the elemental maps of the major elements in the alloy at temperatures obtained from DSC results.	33
19	Mg/Si ratio (length and width) of precipitates presented in CG AA6061 alloy according to temperatures obtained via DSC results. Note: Around 20 precipitates were measured. Smaller precipitates may lead to overestimation of the content of both Mg and Si due to matrix effects.	34
20	The thermogram obtained via DSC from the UFG AA6061 alloy. These experiments were performed with a linear heating rate of $10^\circ\text{C}\cdot\text{min}^{-1}$	35
21	S/TEM micrographs and SAED patterns obtained from the UFG AA6061 alloy at room temperature and at 225°C and 318°C according to the identified DSC peaks in Figure 20.	36
22	The STEM-EDX mapping of UFG AA6061 alloy samples show the elemental maps of the major elements in the alloy at room temperature, 225°C and 318°C according to the peaks obtained via DSC.	37
23	Mg/Si ratio (radius) of precipitates detected in the UFG AA6061 alloy according to temperatures obtained via DSC results. Note: Around 20 precipitates were measured. Smaller precipitates may lead to overestimation of the content of both Mg and Si due to matrix effects.	38
24	Grain size measurements (length and width) for the UFG AA6061 alloy at room temperature and at 225°C and 318°C	39
25	BFTEM micrographs showing <i>in situ</i> TEM experiments conducted as a function of temperature on the UFG AA6061 alloy. Note: Limited precipitation is observed at 250°C , as indicated by the white circles in micrographs, and in which dissolution started at around 316°C	40

List of Tables

2.1	Standard chemical composition of commercial AA6061 alloy (wt.%) [10].	15
3.1	Experimental chemical composition of the commercial CG AA6061 alloy (wt%).	26
4.1	Mg/Si ratio and average size measurements of the precipitates identified in the CG AA6061 alloy.	34
4.2	Mg/Si ratio and average size measurements of the precipitates identified in the UFG AA6061 alloy.	38
6.1	List of artificial intelligence used in this thesis.	57

Acronyms

AA – Aluminium Alloy
APFIM – Atom Probe Field Ion Microscopy
APT – Atom Probe Tomography BF-STEM – Bright Field Scanning Transmission Electron Microscopy
BFTEM – Bright-Field Transmission Electron Microscopy
CG – Coarse-Grained
DSC – Differential Scanning Calorimetry
DFTEM – Dark-Field Transmission Electron Microscopy
ECAP – Equal-Channel Angular Pressing
EDX – Energy-Dispersive X-ray Spectroscopy
FCC – Face-Centred Cubic
GCR – Galactic Cosmic Rays
GP – Guinier-Preston
HAADF – High-Angle Annular Dark Field
HPT – High-Pressure Torsion
OES – Optical Emission Spectrometry
LAADF – Low-Angle Annular Dark Field
LEO – Low Earth Orbit
MEMS – Micro-Electro-Mechanical System
OM – Optical Microscopy
SAED – Selected-Area Electron Diffraction
S/TEM – Scanning and Transmission Electron Microscopy SPD – Severe Plastic Deformation
SSSS – Super Saturated Solid Solution
TEM – Transmission Electron Microscopy
UFG – Ultrafine-Grained
XRD – X-ray diffraction

Abstract

This work explores alloys in the Al–Mg–Si system for application in space. To be considered suitable for space applications, an alloy must meet requirements that include, not exhaustively, high strength-to-weight ratio, high thermal performance, optimal radiation shielding and resistance. Due to its lightweight and high-strength, aluminium and its alloys are considered suitable options. The ability to achieve increased strength via age-hardening, sets aluminium alloys as strategic materials for future space programs. Age-hardening promote precipitation that prevents dislocation motion, thus increasing strength. However, when subjected to space, energetic particle irradiation from the Sun can cause degradation of aluminium alloys as it induces both dissolution of precipitates and formation of extensive networks of dislocation loops. To mitigate the deleterious impact of energetic particle irradiation, one solution has been the development of new ultrafine-grained (UFG) aluminium alloys, where the large amount of grain-boundaries promote the fast-annihilation of radiation damage. Nevertheless, developing an UFG aluminium alloy with high thermal stability against recrystallisation has been a major challenge. For these reasons, this work addresses on the synthesis of an UFG AA6061 alloy using a severe plastic deformation (SPD) technique known as high-pressure torsion (HPT). After demonstrating the feasibility of synthesis, the research investigates the precipitation behaviour in the UFG AA6061 alloy compared with its coarse-grained (CG) counterpart through a combination techniques such as differential scanning calorimetry (DSC) and scanning transmission electron microscopy (S/TEM). Thermal stability of the UFG AA6061 alloy was also investigated via *in situ* TEM experiments.

The findings indicate that the phenomenon of precipitation hardening is highly dependent on the average grain size of the two CG and UFG AA6061 alloys. The phenomenon of precipitation was also demonstrated to be accelerated in the UFG alloy and this was reflected by the fact that intermediate metastable phases such as the β'' were not observed in the UFG AA6061 alloy, and that the equilibrium phase (β), rapidly formed at lower temperatures. It was found via analytical S/TEM mapping techniques that the UFG AA6061 alloy presents limited precipitation ability taking place mainly at intra-granular positions and with low volumetric densities when compared with the CG AA6061 alloy. These characteristics were responsible for recrystallization of UFG microstructure at around of 180°C when tested via *in situ* heating. This thesis highlights the potential of UFG aluminium alloys for application in sapce, but also underlines the difference between the UFG AA6061 alloy and the UFG crossover aluminium alloys, the AlMgZnCuAg, which due to its high volume density of T-phase precipitates and low (highly negative) enthalpy of formation for precipitation (compared to β precipitates in AA6061 alloys) restricts grain boundary movement and delays recrystallisation via intra-granular precipitation and growth.

Kurzfassung

In dieser Arbeit werden Legierungen im Al-Mg-Si System für die Anwendung im Weltraum untersucht. Um für Weltraumanwendungen geeignet zu sein, muss eine Legierung eine Reihe an Anforderungen erfüllen. Dazu zählen unter Anderem ein hohes Verhältnis von Festigkeit zu Gewicht, hohe thermische Leistung sowie eine optimale Strahlungsabschirmung und -beständigkeit. Aluminium und seine Legierungen gelten aufgrund ihrer geringen Dichte und gleichzeitig hohen Festigkeiten als geeignete Optionen. Ihre Fähigkeit, die Festigkeit durch Aushärtung zu erhöhen, macht Aluminiumlegierungen zu strategischen Materialien für zukünftige Raumfahrtprogramme. Die Aushärtung erfolgt über die Bildung von Ausscheidungen, die Versetzungsbewegungen hindern und so die Festigkeit erhöhen. Im Weltraum kann allerdings die Bestrahlung mit energiereichen Partikeln von der Sonne zu einer Schädigung von Aluminiumlegierungen führen. Sie verursacht sowohl die Auflösung von Ausscheidungen als auch die Bildung umfangreicher Netzwerke von Versetzungsringen. Neue, ultrafeinkörnige (UFG) Aluminiumlegierungen bieten das Potential, die schädlichen Auswirkungen der Bestrahlung mit energiereichen Teilchen abzumildern, da die grosse Dichte von Korngrenzen die schnelle Ausheilung von Strahlungsschäden ermöglicht. Die Entwicklung einer UFG-Aluminiumlegierung mit hoher thermischer Stabilität gegen Rekristallisation stellt jedoch eine grosse Herausforderung dar.

Deshalb stellt ein Schwerpunkt dieser Arbeit die Synthese einer UFG-Legierung AA6061 mit der Methode der sogenannten "severe plastic deformation" (SPD), genauer der Hochdrucktorsion (HPT), dar. Die Arbeit umfasst neben einer Machbarkeitsanalyse und der Synthese auch den Vergleich des Ausscheidungsverhaltens in der UFG AA6061-Legierung zu dem grobkörnigen Pendant (CG). Dazu kommt eine Kombination von Techniken wie dynamische Differenzkalorimetrie (DSC) und Raster/Transmissions Elektronenmikroskopie (S/TEM) zum Einsatz. Die thermische Stabilität der UFG AA6061-Legierung wurde auch mittels TEM-Experimenten in-situ untersucht.

Die Ergebnisse zeigen, dass das Phänomen der Ausscheidungshärtung stark von der durchschnittlichen Korngrösse der beiden Legierungen CG und UFG AA6061 abhängig ist. Das Phänomen der Ausscheidungshärtung wurde in der UFG-Legierung nachweislich beschleunigt, was sich in der Tatsache widerspiegelt, dass metastabile Zwischenphasen wie β'' in der UFG AA6061-Legierung nicht beobachtet wurden und dass sich die Gleichgewichtsphase (β) bei niedrigeren Temperaturen schnell bildete. Mittels analytischer S/TEM-Mapping-Techniken wurde festgestellt, dass die UFG AA6061-Legierung im Vergleich zur CG AA6061-Legierung nur eine begrenzte Ausscheidungsfähigkeit aufweist, die hauptsächlich an intragranularen Positionen und mit geringen Volumendichten stattfindet. Diese Eigenschaften führen dazu, dass das UFG Material bei 180 °C rekristallisiert, wie in in-situ Erhitzungsexperimenten festgestellt wurde.

Diese Arbeit zeigt das Potenzial von UFG-Aluminiumlegierungen für Raumfahrtanwendungen, unterstreicht aber auch den Unterschied zwischen der UFG-Legierung AA6061 und den Crossover-

Aluminiumlegierungen AlMgZnCuAg im UFG-Zustand, die aufgrund ihrer hohen Volumendichte an T-Phasenausscheidungen und ihrer niedrigeren Bildungsenthalpie für Ausscheidungen (im Vergleich zu den β -Ausscheidungen in AA6061-Legierungen) die Bewegung der Korngrenzen einschränken und die Rekristallisation durch intragranulare Ausscheidungen und Wachstum verzögern.

1 Introduction

The exploration of the universe has always been a great desire for mankind. The advancement of the human-based space exploration is intrinsically linked to progress in both metallurgy and materials science. In the last decades, these sciences experienced a substantial evolution, and the aim has always been to improving the properties of materials, to make them cheaper, more available, stronger and more reliable.

The progress of metallurgy and materials science was crucial to the success of past space missions as it addressed the unique challenges posed by the earlier developments in aeronautics, astronautics, rocketry, and satellite technology and so on, but with the resumption of many space programs in the last few years, in part driven by the productive sector, but also led at a governmental level by many emerging nations such as China and India [1], new materials challenges considering the extraterrestrial exploration of the solar system as well as possible settlement in these sites are now driving new demands for innovation in space technology, therefore, inaugurating a formal branch for research & development: the space materials.

Within the development of space materials as a topic of scientific research in both metallurgy and materials science, one of the major challenges will certainly be to ensure that future space materials can preserve their designed properties despite the multiple degradation mechanisms operating in synergy and that are inherent to the space environment [2]. Consequently, the development of new space materials is driven by several requirements taking into account these degradation mechanisms that can interact and operate simultaneously during in-service in space. Some of these criteria have been already discussed in literature by Mouritz, Finckenor, Ghidini, Tunes, and Willenshofer [2–6]. In brief, the list of requirements a potential space material must exhibit include, not exhaustively: (i) strength-to-weight-ratio, (ii) thermal performance, (iii) corrosion protection, (iv) radiation shielding and tolerance, (v) mechanical damage tolerance, and the triad of (vi) availability, manufacturability, and (low) cost.

Considering the high and strict standards on the design and selection of space materials, aluminium is considered a critical metal for space and it is already in-use in many satellites and spacecrafts primarily due to its high strength-to-weight ratio, but also due to its ability to be manipulated and optimised to achieve high strength through alloying and precipitation hardening, which is advantageous considering the list of requirements aforementioned. Perhaps the most rigorous example of the successful use of aluminium and its alloys in space is in the former NASA's Space Shuttle programme, where the metal was used in a variety of forms including sheet, wire, web, honeycomb, cold and hot formed structures, as shown in figure 1.

With respect to the application of aluminium alloys in space, and mainly considering future long-term human-based space missions with possible definitive human settlement in extraterrestrial locations, the principal challenge that remains open for science is on radiation damage. In

our solar system, radiation damage is caused primarily by the impact of highly energetic particles emitted from the Sun during solar flares and coronal mass ejections, and also arising from cosmic origins as in the case of galactic cosmic rays [7].

Considering the effects of irradiation in existing aluminium alloys, radiation damage primarily causes alloy softening, a phenomenon that takes place by the irradiation-assisted dissolution of hardening precipitates [2, 6, 8–10]. Upon impact into the aluminium alloy microstructure, these energetic particles have sufficient energy to drive ballistic dissolution of precipitates [11]. The alloy softening effect may worsen upon radiation dose accumulation during the long-term operation of the aluminium-based structure in space. For long-term human-based space missions, the development of radiation-resistant aluminium alloys emerges as a new topic of research within the metallurgy of lightweight non-ferrous alloys and it was recently inaugurated by our research group at the Montanuniversität Leoben [2].

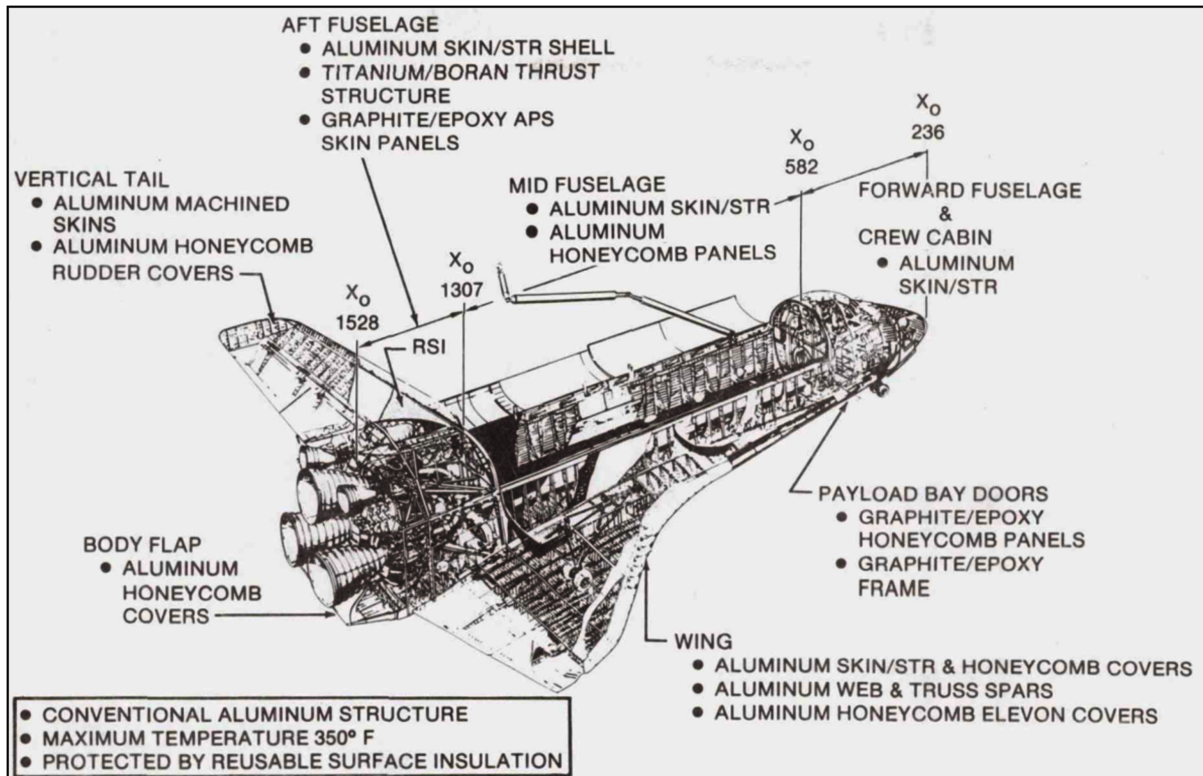


Figure 1: The NASA's space shuttle program used aluminium and its alloys in several forms spread all over the design and fuselage of the multiple spacecrafts [12]. Note: Reproduced from work performed by the U.S. Government, public use permitted.

Given the above considerations and the necessity to improve radiation resistance in aluminium alloys, our group engaged in this research and discovered in 2020 that the new Al–Mg–Zn aluminium crossover alloys [13], a metallurgical merge between 5xxx and 7xxx aluminium alloy series [14, 15], features a hardening precipitate – the T-phase with $Mg_{32}(Zn,Al)_{49}$ – that is able to resist ballistic dissolution at higher irradiation dose levels when compared with data available for the the conventional and commercial Al–Mg–Si (AA6061), one of the most used aluminium

alloys in space [10]. However, during the irradiation studies, the crossover alloy experienced accumulation of radiation damage in the microstructure in a form of dislocation loops, which can be deleterious for the mechanical performance of the alloy when under in-service conditions.

To address on this latter problem, the proposed solution has been the synthesis of crossover aluminium alloys with a stable UFG microstructure [2, 6, 16, 17]. Grain-size reduction towards UFG and nanocrystalline microstructures is a long-standing strategy to improve several materials' properties, including the radiation resistance of nuclear materials [18]. The large number of interfaces – such as grain boundaries – that are inherent to UFG alloys contribute to increase the defect sinking efficiency as predicted theoretically in the 1970s by a British team led by Bullough *et al.* [19, 20]. Recent radiation tests in this latter UFG crossover alloy have demonstrated high radiation tolerance, manifested by the absence of dislocation loops in its grains, no recrystallization and survivability of T-phase precipitates up to very high doses, therefore, this new alloy presents a stable UFG microstructure [6, 16, 17].

Although our group has been focusing into the development of crossover aluminium alloys for space, both irradiation and thermal stability data on an UFG version of the AA6061 alloy remains to be performed and this is of paramount importance to confirm (or not) the advantages of crossover aluminium alloys when compared to existing commercial alloys considering possible application in space. Given the facts presented above, the objective of this master thesis is to synthesise the AA6061 UFG aluminium alloy derived from the commercial CG alloy. This UFG alloy was synthesised via HPT and the the desired UFG structure was achieved. The resultant samples and the as-received samples were analysed and characterised using DSC and S/TEM to evaluate the behaviour of precipitates in both UFG and CG samples. Additionally, the synthesized UFG alloy thermal stability was assessed through *in situ* TEM heating. It will be demonstrated that this alloy can be produced, characterised and that it is ready for further radiation testing following this work.

2 Literature review

2.1 Space materials and the choice of aluminium

2.1.1 Requirements for space materials

To be used in space, a material must meet some requisites considering the different types of degradation forces that may be present in this environment. These degradation mechanisms and their effects on materials were recently reviewed by many authors such as Mouritz, Finckenor, and Ghidini [3–5]. Tunes *et al.* and Willenshofer *et al.* [2, 6] recently summarised the remaining materials challenges that involves the application of metallic alloys in the space environment, with a focus in aluminium alloys. Overall, the materials to be applied in space must exhibit the following desired properties:

- **Strength-to-weight ratio:** Materials intended for use in space must have high mechanical strength and at the same time be lightweight. Optimal space materials exhibit both high strength and reduced weight. Light-weightness is an important characteristic that space materials must exhibit in order to reduce the payload and costs of a space mission [21].
- **Thermal performance:** Materials must withstand high variations in temperature maintaining excellent mechanical performance. Suitable thermal performance must also reflect in functional parameters including heat capacity, thermal conductivity, cryogenic response, and thermal expansion. In addition, cycling thermal stress can cause thermal fatigue in materials and this topic must be addressed during the design stage of a spacecraft or satellite component.
- **Corrosion protection:** In low Earth orbit conditions (LEO), materials must resist the corrosive action of monoatomic species, such as oxygen and hydrogen, present in the ionized plasma at high altitudes near Earth.
- **Radiation Shielding and Tolerance:** In the space environment, a material may be subjected to high levels of charged particle radiation (*e.g.*, protons, He^+ , galactic cosmic rays (GCRs), etc.) and also ionizing radiation (*e.g.*, gamma rays, X-rays, infra-red and ultra-violet as electromagnetic waves etc.) [7]. These radiation fields must be appropriate shielded following the ALARA principle [22, 23] – as low as reasonable achievable – therefore, the design of space materials must consider both shielding effectiveness and radiation damage tolerance.

- **Mechanical damage tolerance:** The material must exhibit both high fracture toughness and suitable ductility to prevent crack propagation and failure, especially considering the high-strain rates posed by impacts in space. These impacts can be against micrometeoroids and space debris (space junk) [24].
- **Availability, manufacturability, and cost:** Space programs demand constant and long-term supply of materials. Cost-effectiveness and efficiency considerations in the manufacturing process are crucial. This includes several stages, such as purchasing, processing, machining, forming, heat treatment, inspection, maintenance, repair, and replacement. In space, repairability of spacecraft and satellite components and fuselage is limited, therefore, materials to be applied in space must be easily replaced and/or repairable.

Understanding the synergy between these requirements is essential for the development and progress of space materials technology. There is an extraordinarily large number and variety of materials available to build spacecrafts and satellites. It is estimated that there are more than 120,000 materials that can be used, including metals, plastics, ceramics, and composites, however, only a small portion of the materials are suitable for spacecraft application due to their ability to meet the demanding requirements aforementioned. [3] The main groups used in aerospace applications are aluminium and titanium alloys, steels, and composites [3]. The materials used need to be developed with strict quality requirements that would allow them to remain stable on a lasting basis [25].

2.1.2 Challenges for aluminium in space

Within the above-mentioned materials and requirements, aluminium emerges as a preferred option for space applications, primarily due to its strength-to-weight ratio, but also higher-strength when alloyed, suitable manufacturability and market availability [2]. In fact, aluminium alloys are widely used in space applications for more than 80 years [25], and the first human-made satellite – the Sputnik-1 – was essentially a polished sphere made of aluminium [26]. For all these reasons, aluminium has a prospective future in the space section sector. By 2025, it is expected that a global demand of 80 million metric tons of cumulative production will be reached for this industry alone [10].

Due to their higher strength, aluminium alloys – instead of pure aluminium – are currently employed in numerous spacecraft and satellite and they serve a dual role of being a structural material that, at the same time, provides shielding against both energetic particles and electromagnetic radiation. This space radiation is deleterious for materials as it deposits energy in their crystalline structure causing radiation damage, which can significantly act as a limiting factor for application of aluminium alloys in space. Most aluminium alloys in space are age-hardenable, which means that to achieve high-strength, they are thermally treated to promote precipitation. These precipitates act as barrier for dislocation motion, thus increasing mechanical properties of

pure aluminium. Highly energetic solar protons emitted by the Sun can impact the microstructure of age-hardenable aluminium alloys promote dissolution of precipitates [2, 6]. Upon dissolution, the aluminium alloy loses its initial strength, which can result in catastrophic failures for a space program and jeopardise the safety of human-crew and communication satellites.

2.1.3 Brief overview of the irradiation effects in aluminium alloys

The literature on the effects of irradiation in aluminium alloys is sparse and it is by many authors considered limited [2, 27, 28]. Due to its low melting point, aluminium is not used in nuclear power reactors. Although some aluminium alloys are indeed used in nuclear research reactors operating at room-temperature [29, 30], up to date, there was no strict demand for a systematic research program addressing on radiation damage in aluminium alloys.

The core research on the effects irradiation on aluminium alloys has been focused into the following aluminium alloy (AA) systems: Al-Cu (AA2xxx) [31–33], Al-Zn (AA7xxx) [34], Al-Mg (AA5xxx) [35] and the Al-Mg-Si (AA6xxx) [36, 37]. Tunes commented that such literature on radiation effects of aluminium alloys is largely scattered considering the type of irradiation, *i.e.*, neutron and/or ions, and the irradiation conditions, such as flux, dose, temperature etc [2]. Therefore, with regards to the application of aluminium alloys in space, the existing literature only provide a marginal idea of what happens with the microstructure and properties of a certain aluminium alloy in irradiation environments.

Considering the impact of highly-energetic protons into the microstructure of commercial aluminium alloys, a scenario that directly emulates the effect of Solar radiation in metallic alloys, in late 1980s, a research group lead by W. Sommer at the Los Alamos National Laboratory (USA) and by W. Lohmann at the Forschungszentrum Jülich (Germany) decided to study the effects of proton irradiation into Al-Mg alloys, and especially Al-Mg-Si alloys: the latter commercially known as AA6061 [8, 9]. For these studies, the authors have used the 800 MeV proton beam line at the Los Alamos Meson Physics Facility (LAMPF)¹. Lohmann *et al.* [8, 9] reported to the scientific community that upon impact of high-energy protons, the hardening precipitate of the AA6061 alloy when in the temper T6, the Mg₂Si known as β -phase, faces complete dissolution at irradiation doses as low as 0.2 dpa (displacement-per-atom²). The unit dpa means that one atom in the crystalline structure of the β -phase was (on average) displaced from its equilibrium lattice site at least 0.2 times, which was found by the authors to be sufficiently high to dissolve such precipitates. The dissolution of these precipitates – also observed in the Al-Mg alloy – was reflected on a severe loss of strength, understood as an alloy “softening” effect.

It is worth emphasising that the AA6061 alloy is considered nowadays, one of the most used aluminium alloy in space [10], therefore, the previous works by Lohmann *et al.* [8, 9] bring

¹Nowadays known as Los Alamos Neutron Science Center (LANSC).

²With respect to the dose unit, 1 dpa of irradiation dose in materials means that the atoms in lattice sites were averagely displaced at least one time.

immediate attention to the safety and reliability of spacecrafts and satellites made using this alloy as major structural material.

2.1.4 The advent of radiation-resistant aluminium alloys

With the advent of space exploration and mankind's aspiration to initiate extraterrestrial settlement, the topic of radiation-resistant aluminium alloys has been revisited by our Chair of Nonferrous Metallurgy in 2020, and both a research line and task-force for the search of new aluminium alloys capable of resisting the deleterious effect of space radiation have been created here in Leoben.

In face of the dissolution of hardening precipitates in the AA6061 in irradiation doses as low as 0.2 dpa, as reported by Lohmann *et al.* [8], our group decided to test the survivability of T-phase precipitates within the new Al-Mg-Zn crossover alloy. The results reported in 2020 show T-phase can survive up to a dose of 1 dpa [2], which is 5 times higher than the β -phase in the commercial AA6061 alloy, as can be seen in Figure 2. It has been proposed that the origin of the radiation resistance of T-phase precipitates is due to the fact that this phase can form in these new crossover aluminium alloys at higher volumetric densities than compared to the β -phase in the commercial AA6061 alloy, which would help to sink excess point defects generated by the events of irradiation.

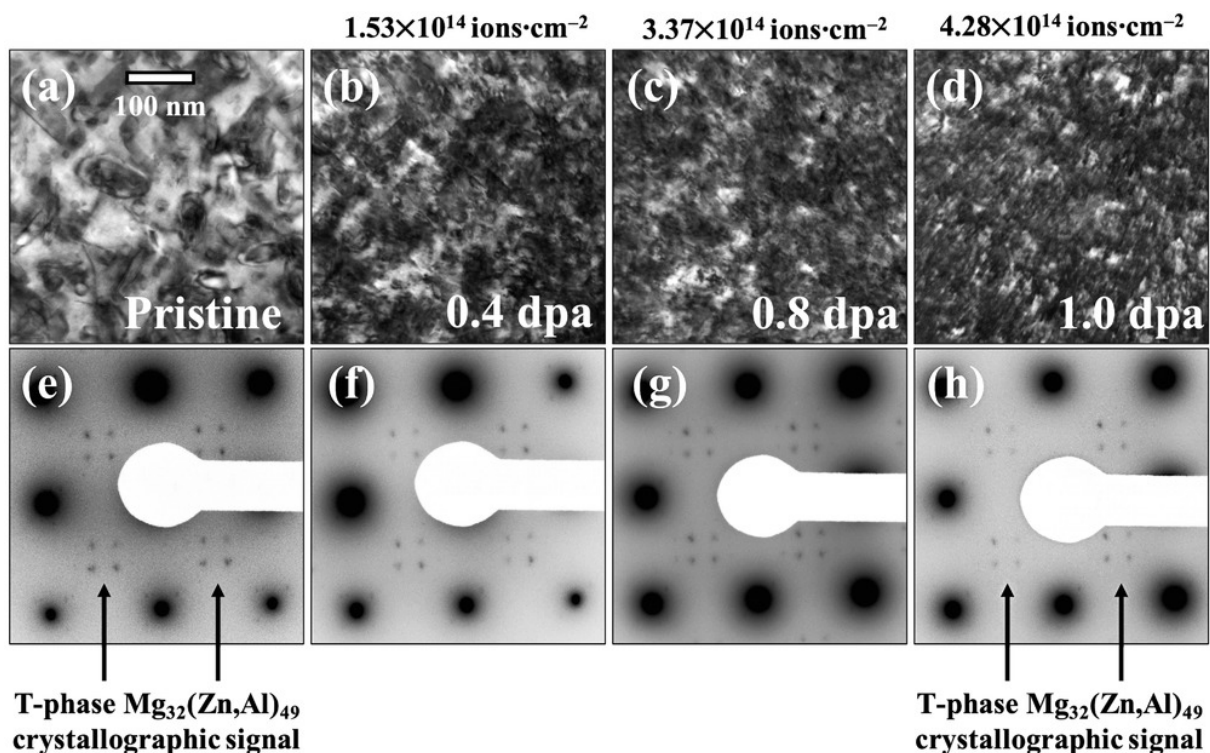


Figure 2: T-phase precipitates were observed to survive to irradiation doses around 1 dpa. In the figure, the survivability of the T-phase was attested by monitoring its diffraction signal in the alloy's diffraction pattern as a function of the irradiation dose. Note: Reproduced from the open access paper by Tunes *et al.* [2].

On the effects of irradiation on new aluminium crossover alloys, in the Figure 2, it is evident that displacement damage in a form of dislocation loops have extensively accumulated in the alloy's microstructure. This is noted by observing the particular "black" contrast build-up in the bright-field TEM (BFTEM) micrographs. Although the T-phase precipitates have not dissolved, thus ruling out the phenomenon of alloy softening, the accumulation of dislocations may drive the alloy to an brittle state, as irradiation is known to cause hardening in metals and alloys [38].

By studying the effects of irradiation on aluminium crossover alloys commensurate with the existing – but limited – literature on the effects of irradiation in commercial aluminium alloys, Tunes *et al.* defined the following criteria must be addressed considering the future design of aluminium alloys for space applications [2]:

- Hardening phases able to resist ballistic dissolution; and
- An alloy matrix that mitigate the formation of displacement damage in a form of voids and dislocations;

Although a complete overview on the radiation survivability among the major hardening phases in the wide spectrum of existing aluminium alloys is currently not available, the performance of T-phase as a hardening precipitate in irradiated aluminium alloys currently scores a record [2, 6]. Nevertheless, in order to reduce the amount and build-up of dislocations in the matrix grains during the events of energetic particle irradiation, the idea of producing UFG and nanocrystalline aluminium alloys have been given by Tunes in 2020 [2].

2.2 Ultrafine-grained aluminium alloys

Reducing the grain size of aluminium alloys towards nanocrystallinity emerges as a potential strategy to reduce the dislocation build-up in matrix grains due to irradiation [2, 18]. Over the past years, techniques involving the application of the SPD principle have been shown to produce nanostructured aluminium alloys [39–43] and it will here briefly reviewed with focus on HPT, as this is the major technique employed in this work to synthesise the AA6061 in the UFG form.

2.2.1 The principle of severe plastic deformation

Historically, several procedures and techniques have been developed with the major purpose of reducing the grain size from micrometer to nanometer levels and with the final aim of improving both the physical and mechanical properties of metallic alloys.

SPD is form of a metal-forming technique characterised by the application of high hydrostatic pressure. There are several different techniques that employ SPD to refine metallic alloys' grain sizes, as can be seen in Figure 3 [43]. SPD methods typically subject solids to very high

stresses without substantially altering the overall dimensions of the sample and are well known for their ability to achieve exceptional grain refinement in materials [44].

Several mechanisms can be involved during grain refinement via SPD methods that change the final properties of an alloy system. For example, Hall-Petch [45, 46] relationship reveals that by reducing the grain size, the strength of the alloy can be significantly increased. This emphasises that the modern application of SPD methods in metallic alloys is not only to produce radiation-resistant alloys, but also for improving many of the alloys' properties.

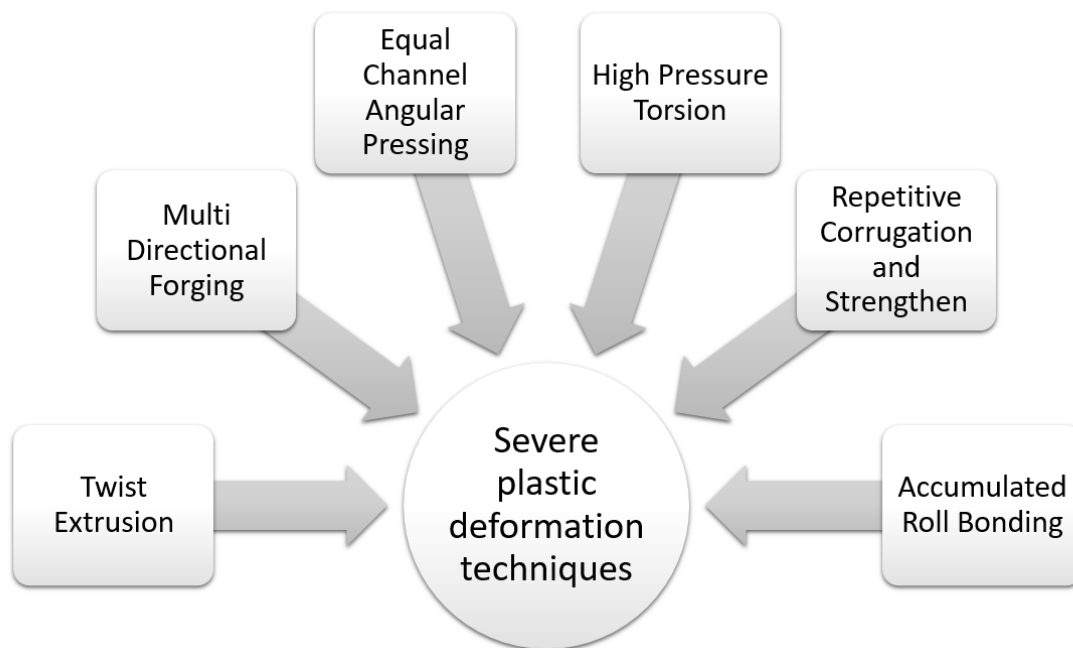


Figure 3: Graphical representation of SPD techniques. Note: Redrawn and reproduced from [43].

Within the grain refinement mechanism, lies the principle that the shear stress applied to the sample increases the dislocation density and forms dislocation walls; and as a result, one may obtain a low-angle grain boundary. The final shape and size of the grains formed can change owing to the specific SPD process and the parameters used such as strain and temperature [47].

An important remark must be made with respect to the SPD application on aluminium alloys. Reducing the grain size to a nanometer scale can modify how precipitation can occur and, consequently, alter the precipitation sequence in an aluminium alloy [16]. Ultimately, this has an impact on the mechanical properties of the bulk nanostructured material. By subjecting an aged aluminium alloy containing pre-existing precipitates to SPD, these precipitates can undergo fragmentation or dissolution within the matrix. This process results in the material adopting a supersaturated solid solution state (SSSS). Conversely, in the absence of pre-existing precipitates, SPD can trigger dynamic precipitation in a material already in the SSSS state [16].

Unlike conventional techniques such as nano-powder compaction or gas condensation, the SPD methods are particularly suited to produce samples without porosity. The existing literature has proved the ability of the SPD process to produce UFG microstructures with sub-grains in a

wide spectrum of materials, including pure metals, their alloys and intermetallic forms [47, 48].

Nanostructured alloys created by SPD are widely recognised for their many superior properties [39–43]. For example, in the case of UFG aluminium alloys, research has shown that they can exhibit mechanical strengths 1.2–2.0 times higher than their coarse-grained (CG) counterparts when processed by standard ageing treatments [49, 50]. In addition, several studies have shown that properties such as ductility, fracture resistance, electrical conductivity, and corrosion resistance can also be improved [49].

Nanostructured alloys processed via SPD methods can also act as functional materials. Applications ranging from sport equipment, electronic, micro electro-mechanical systems (MEMS), oil, gas, and energy sectors, biomedical devices, aerospace and transportation industry have been reported [50].

2.2.2 High-pressure torsion

In HPT, a thin disc-shaped sample is held between two large anvils, thus subjecting it to simultaneous high hydrostatic pressure and torsional stress. The process of HPT is shown in Figure 4. In HPT, a large amount of deformation can be imposed in a single deformation step due to the high hydrostatic pressure applied. [51]

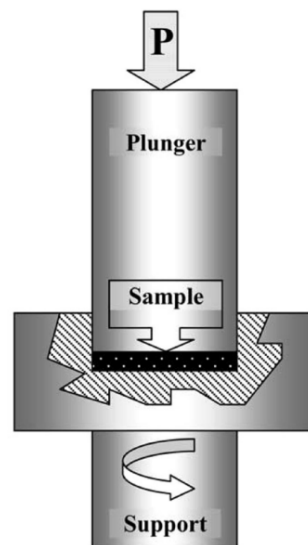


Figure 4: Schematic illustration of HPT processing. Note: The drawing was extracted from Zhilyaev *et al.* [52].

The shear strain generated in this method is calculated as follows in Equation 2.1:

$$\gamma = \frac{2\pi r N}{h} \quad (2.1)$$

In equation 2.1 r represents the distance to the centre of the disk, N the number of turns, and h the thickness of the disc [43, 53].

Some advantages of HPT when compared with the many SPD methods can be noted. Firstly, it is easier to adjust the processing factors such as pressure, temperature, strain and strain rate. With this technique, it is possible to alter the angle of rotation, thus the shear stress can be increased in very small steps. Secondly, due to the high pressure used in HPT, it is possible to process a wide range of materials, even if initially brittle [43]. Despite these advantages, samples deformed with HPT are usually smaller than those deformed with other techniques, which means significant limitations when applied in industrial scale. In addition, HPT setups can be more complex and costly compared with other SPD methods [43].

2.2.3 The thermal stability challenge for UFG aluminium alloys

After the synthesis of a nanostructured aluminium alloy, the major challenge on the possible application of UFG aluminium alloys in space is their thermal stability (for instance, not considering radiation effects post alloy processing). Valiev and Landgon summarised the results of multiple experiments that used *in situ* TEM heating to probe the stability of some select UFG alloys [54]. Both UFG pure aluminium and AA7xxx alloys recrystallises at temperatures as low as 200°C [54]. One may understand that if an UFG aluminium alloy recrystallises at low temperatures, it will lose the initial designed property of sinking radiation-induced effects at the grain boundaries.

Recently, Willenshofer *et al.* synthesised a new UFG crossover alloy composed of AlMgZn-CuAg and tested its stability over temperature using *in situ* TEM [6]. The alloy was observed to be stable up to 280°C with slow grain-growth rates at temperatures beyond 300°C [16]. This apparent “delayed” recrystallisation kinetics was attributed to the precipitation and thermal stability of T-phase precipitates along trans- and intra-granular positions [16], an effect that was not previously reported. As can be seen in Figure 5, T-phase precipitates were then discovered to pin grain boundaries at the nanoscale and impede recrystallisation at normal temperatures experienced by UFG aluminium and some of its commercial alloys [54]. Question remains whether an UFG alloy made in the Al–Mg–Si system (*e.g.*, AA6061) would exhibit similar response to the new UFG crossover alloy synthesized by Willenshofer *et al.* [17].

2.3 The Al–Mg–Si system and the AA6061 alloy

The AA6061 aluminium alloy is one of the most used commercial aluminium alloys of the Al–Mg–Si system and features Mg and Si as major alloying elements. When in temper T6, the AA6061-T6 is a heat-treated and precipitation-hardened aluminium alloy that has been found to be a promising material that can meet the requirements of the aerospace industry [10, 55]. This alloy is specifically used to fabricate wings, fuselages and fuel tanks, and also for spacecraft machined-structures and satellites [10, 56].

As defined by standards, the AA6061 alloy composition (wt %) used in space applications is given in Table 2.1. [10]:

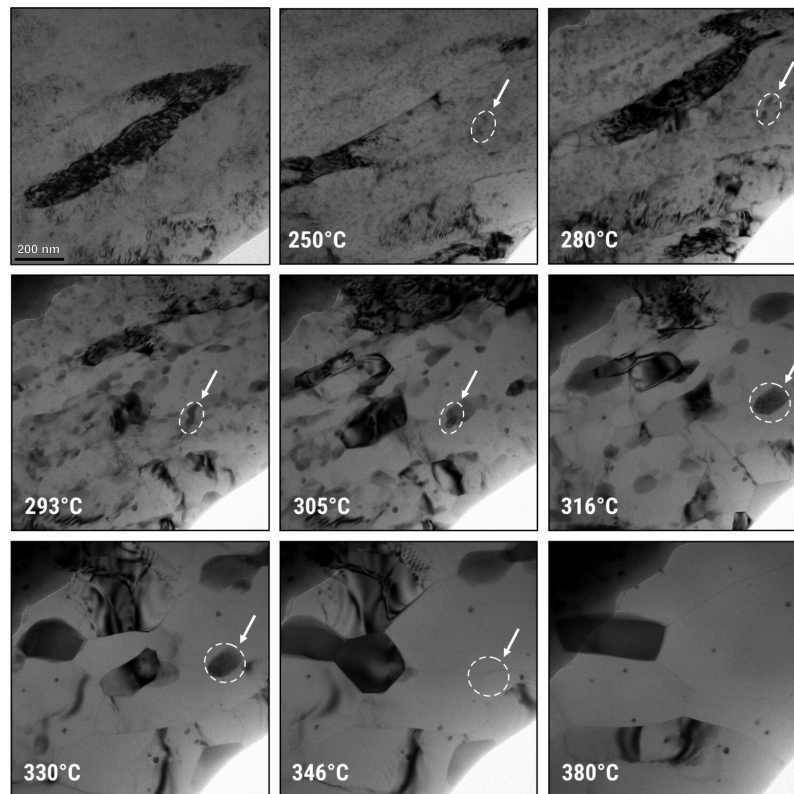


Figure 5: A new UFG crossover alloy made with AlMgZnCuAg was recently show to present superior thermal stability than pure UFG aluminium and some select UFG aluminium alloys made from commercial counterparts. In the figure, BFTEM micrographs show the UFG microstructure as a function of temperature where it is possible to note the action of T-phase precipitates in pinning grain boundaries. Note: Figure was reproduced from the open access paper by Willenshofer *et al.* [16].

Alloy	Cu	Mg	Zn	Mn	Si	Fe	Cr	Ti
AA6061	0.15-0.4	0.8-1.2	0.25max	0.15 max	0.4-0.8	0.7 max	0.04-0.35	0.15 max

Table 2.1: Standard chemical composition of commercial AA6061 alloy (wt.%) [10].

The addition and concentration of each alloy element play an important role in the final alloy's characteristics and properties. Except to Zn and Ti which are regarded as minor impurities, the role of each alloying element can be clarified as follows [10, 57]:

- **Mg:** Increases the alloy' yield strength upon solid solution hardening and further heat treatment;
- **Si:** Upon heat treatment and combined with Mg promotes the precipitation of the β -phase, or Mg_2Si ;
- **Cu:** Promotes clustering due to a refinement of the cluster/precipitates morphology increasing strength after solution annealing, water quenching and subsequent age hardening [57]; and

- **Mn, Fe, Cr:** Promote the formation of stable dispersoid phases formed after casting which are thermally stable after homogenisation treatment with a minor impact in the alloy's overall mechanical response and properties.

The standard process for manufacturing 6xxx series heat-treatable aluminium alloys has been described by Baruah *et al.* [58]:

1. Casting: The production of Al alloys begins with the creation of ingots, primarily through casting. In this process, aluminium is melted, and it is crucial to perform fluxing or degassing to remove slag, oxides, gases, and non-metallic impurities, ensuring a high-quality cast product [58].
2. Homogenisation: This treatment is applied to castings at elevated temperatures between 530-600°C, below the melting point of the aluminium alloy. The primary goal is to homogenise the structure and eliminate elemental segregation, resulting in a uniform distribution of alloying elements and other constituents [58, 59].
3. Hot Working: This process converts cast and homogenized ingots into wrought products like sheets, plates, rods, and tubes. During hot working, such as rolling and extrusion, plastic deformation occurs. The material must be reheated after each deformation step to continue plastic deformation. The final result of hot working typically has a poor surface finish.
4. Cold Working: To improve surface finish and strength, hot-worked aluminium alloys are cold-worked at room temperature;
5. Annealing: To remove defects caused by cold working and to soften the aluminium alloy, annealing is performed; and
6. Ageing Treatment: The strength of aluminium alloys increases due to precipitates formed during thermal treatment. Alloys that undergo ageing may harden at room temperature, known as "natural ageing", which can continue for a long time, though the rate slows significantly after months or years. Ageing at higher temperatures ("artificial ageing") leads to an initial increase in hardness, reaching a peak, followed by a decrease, termed "overageing". The peak hardness occurs at a specific temperature unique to each alloy. In commercial alloys like AA6061, maximum hardening occurs in temper T6, with solid solution hardening in T4 and overageing in T7.

The stages of this ageing/thermal treatment have to be discussed in more detail as follows [57, 58, 60, 61]:

1. Solution treatment at a relatively high temperature in the range of 520–570°C within the single-phase region;

2. Rapid cooling or quenching, typically to room temperature, is used to attain an SSSS; and
3. The controlled decomposition of the SSSS leads to the formation of a finely dispersed precipitate, usually achieved by aging at room temperature or by artificial ageing at intermediate temperatures ranging from 160–200°C.

To really understand what happens during the aging process of Al-Mg-Si alloys, it is necessary to analyse the precipitation sequence of the AA6061 alloy, which is often determined by thermogravimetric methods such as DSC. For the AA6061 alloy, the precipitation sequence is complex and it has been extensively studied in literature [62]. Dumitraschkewitz *et al.* summarised the state-of-the-art on the steps in this sequence whose can be enumerated as follows [62]:

1. Quenching the solution-treated alloy to retain a SSSS;
2. Formation of Si and Mg clusters;
3. Clusters evolve to pre-Guinier-Preston zones I (GP-I) known as pre- β'' ;
4. Formation of β'' ;
5. Metastable β'' evolves to β' ;
6. Metastable β' evolve to B' (some intermediate phases U1 and U2 are reported during this step [62]); and
7. Metastable B' stabilises to the β -phase (Mg_2Si) plus Si.

There is also evidence to indicate that precipitates other than those listed above may form [62, 63]. The complete decomposition of an SSSS is typically a complex process that often occurs in multiple stages [61].

The precipitation starts with individual solute clustering of Si and Mg at the atomic level, but the structure is generally considered only in theoretical terms due to the difficulties in the experimental characterisation and analysis of early-stage clustering. Co-clusters form after the dissolution of Mg clusters [60]. In contrast to co-clusters, GP-I zones are more thermally stable, contain more solute atoms and are of spherical-shape, with a typical size from 1 to 3 nm. The GP-I zones represent the initial type of precipitate in the sequence, providing a clear contrast for identification by TEM via strain-field contrast [63]. Generally, all precipitates in the initial GP zone phase are fully coherent, metastable and have all atoms located at (or very close to) the face-centred cubic (FCC) aluminium lattice sites [58, 60, 64]. The solute clusters, on the other hand, are defined solely as regions of higher solute concentration compared to the random distribution in the matrix [64], however, according to Dumitraschkewitz *et al.* the definition of clustering in aluminium alloys is currently subjected to intense debate [62].

The strength of Al-Mg-Si alloys is enhanced by the formation of fine precipitates of Mg and Si during the solid-solution phase. These alloys experience substantial hardness increase when a

combination of a large number of fully coherent GP-I zones and a semi-coherent GP-II zones (β'' - Mg_5Si_6 phase) both existing as needle-like structures [65].

The β'' is a phase aligned along the [100] direction of aluminium, it features monoclinic structure and it is fully coherent along the needle axis. The β'' was first discovered by X-ray analysis, and subsequently studied by TEM [63]. They oscillate between 20 and 100 nm in length, and are approximately 6 nm in diameter. They produce "streaks" parallel to [100] directions on diffraction patterns obtained by TEM [60, 63, 65, 66]. The rod-shaped phase β' is formed consecutively by nucleation and growth controlled by diffusion processes. These phases are typical of overaged microstructures [60, 66].

The platelet-like equilibrium β -phase Mg_2Si is formed after age hardening, which has an anti-fluorite structure [58, 60, 61]. This precipitate will form in large volumetric fraction, hindering the movement of dislocations and producing a significant increase in the hardness of the alloy material [58, 64].

Although it is not confirmed, the β^n -phases do not contain Al in its composition. It is generally observed that during the process of heat treatment, succeeding β^n -phases exhibit a higher magnesium content compared to their predecessors. As a result scientists expect that there are additional phases in this sequence as a portion of Si must have been initially removed from the solution at a significantly faster rate than Mg. The sequence also depends on the initial composition of the alloy. At equilibrium, when the final phase β (Mg_2Si) is reached and no remaining excess Mg is in solution, then, if the overall Mg/Si ratio is <2 , Si crystals will coexist with β [62].

Now that the AA6061 synthesis and processing has been introduced, a brief literature review on CG and UFG AA6061 alloys will be given with focus both on the age-hardenability of the alloys when in such microstructural morphologies as well as in the previous work performed on the application of SPD techniques to produce an UFG structure within the Al–Mg–Si system.

2.3.1 Coarse grained AA6061

Dutta *et al.* [67] used both DSC and TEM to study the precipitation evolution of the AA6061 alloy. Their results are herein reproduced in Figure 6. According to the results of the DSC plots, they found four exothermic peaks. The first at 88°C and a high density of small precipitates that are fully consistent with the matrix, suggesting that this peak is related to the formation of Si clusters. The second seems to have two partially overlapping peaks at 241.8°C, peak 2a consists mainly of dot-like and some needle-like precipitates, and a peak 241°C, they found needle-shaped precipitates and superstructure spots visible in the corresponding selected-area electron diffraction (SAED) pattern suggesting an ordered, at least partially coherent, needle-shaped phase, corresponding to GP-II zones or β'' . The third peak at 291°C shows that the GP-II needles have grown into rods and in the SAED pattern is also evident the formation of precipitates with defined order and structure, suggesting that these rod-like precipitates correspond to β' formation. Regarding the fourth peak at 493°C denoted as peak c, the authors presented neither BFTEM micrographs nor SAED pattern,

although they mentioned this peak corresponds to the equilibrium phase, *i.e.*, the β -phase (Mg_2Si).

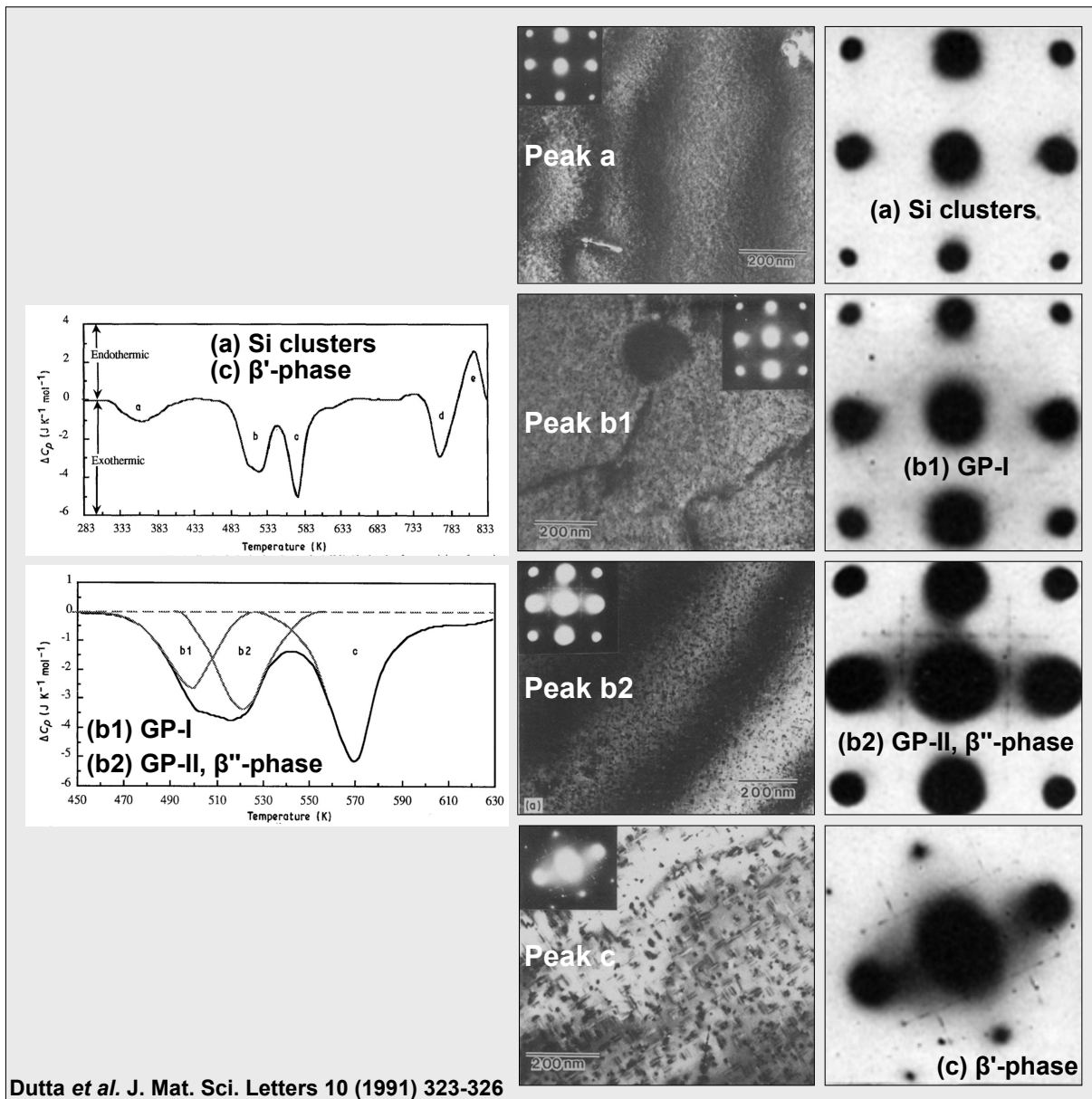


Figure 6: DSC and TEM characterisation data obtained by Dutta *et al.* [67] in the commercial CG AA6061 alloy. Note: Montage made with the original DSC plots, BFTEM micrographs and SAED patterns from the work of Dutta *et al.* [67]. Note: Reproduction granted by Springer Nature.

Following Dutta *et al.* [67], Edwards *et al.* [63] also studied the precipitation of the AA6061 alloy using DSC, TEM and atom probe field ion microscopy (APFIM). These latter authors found that the DSC curve is similar to the Dutta *et al.* [67], but the peaks were observed to be shifted to lower temperatures. This is because a slower heating rate ($5^\circ\text{C}/\text{min}$) was used for these measurements. All the peaks were analysed by TEM, and it was found that in the first peak (specimen heated to 100°C) there is no evidence of any precipitation, but the APFIM showed the presence of clusters of Si atoms, clusters of Mg atoms, and co-clusters containing both Mg and Si atoms. The second

peak shows two overlapping peaks, where small precipitates were observed with no detectable diffraction effects on SAED patterns, therefore with no clear structure. With APFIM it was possible to see that these precipitates contain both Mg and Si. In the case of the peak corresponding to the specimen heated to 250°C, needle-shaped precipitates were observed, and in the SAED patterns taken along with the [001] zone axis, superlattice spots were visible suggesting the presence of the β'' precipitates. In peak corresponding to the specimen heated to 320°C, rod-shape precipitates aligned along [001] direction were observed and superlattice peaks were visible on SAED patterns, pointing to the presence of both β' and B' . Similarly to Dutta *et al.*, Edwards *et al.* have not analysed the highest-temperature peak.

2.3.2 Ultrafine-grained AA6061

Mohamed *et al.* [68] studied strengthening in the AA6061 alloy via grain refinement using HPT and fine precipitation by subsequent ageing treatment. The material was processed under an applied pressure of 6 GPa for 0.75, 1, and 5 turns at a rotational speed of 1 rpm to study the effect of deformation. SAED patterns were taken around the regions of interest and upon analysis it was observed that the patterns displayed less spots at lower strains demonstrating the presence of larger grains [68] *i.e.*, an uniform UFG structure was not obtained. Energy-dispersive X-ray spectroscopy (EDX) mapping revealed the presence of particles rich in Si, Fe, Cr, and Mn. These particles were present in both the solution-treated and HPT-processed samples, suggesting that they were not formed during the aging process, thus resembling to stable dispersoid phases. After HPT processing, the fraction of these particles decreased significantly due to their dissolution in the matrix, and the occurrence of hardening precipitates were not reported in the study [68].

Roven *et al.* investigated the precipitation behaviour during equal-channel angular pressing (ECAP) performed at room temperature and 175°C in an as-cast and homogenised Al-Mg-Si alloy (AA6063) [69]. It was found that fine spherical β'' with an average diameter of about 4 nm are dynamically formed during the SPD process at RT and also at 175°C. The simultaneous observation of β'' precipitates and dislocations indicates that the precipitates readily form around or near dislocations during ECAP. This suggests that ECAP-induced dynamic ageing which is likely facilitated by dislocations [69].

Sha studied the effects of HPT processing on an Al-Mg-Si alloy (AA6060). It was found that under HPT processing the dynamic precipitation of the AA6060 is highly dependent on temperature, duration and applied strain. To facilitate the transformation of small GP zones into small β'' precipitates, a change in crystal structure and chemistry is needed. HPT was found to induce high density dislocations that act as preferential sites for β'' nucleation upon HPT processing temperatures, these results are similar to those observed in these alloys processed by ECAP. [70] It was also found that the use of HPT processing with temperatures between 100-180°C could affect the precipitation sequence by reducing the critical size for GP zone formation and promoting the early transformation of β'' into β' and β [70]. No complimentary SAED patterns were given by

these latter authors to corroborate the identification of precipitated phases.

Singh *et al.* [71] investigated the effect of cryo-rolling in improving strength and ductility in the UFG AA6061 alloy. The performance of the cryo-rolled UFG alloy was investigated following hot-rolling and short-annealing treatments were compared. They used TEM, X-ray diffraction (XRD) and DSC to investigate the precipitation behaviour in the UFG AA6061 alloy. In their work, the CG alloy counterpart was not analysed by TEM, and some of the “claimed” DSC peaks are questionable due to low signal-to-noise ratio. In addition, elemental quantification of Mg/Si ratios via EDX is not provided. They claimed the presence of β'' phase, but only based in previous literature data, *i.e.*, no clear experimental evidence has been provided to confirm it the β'' , such as X-ray diffraction as well as elemental quantification via EDX for Mg/Si ratio etc. It is important emphasising that these authors have not investigated the thermal behaviour of the UFG AA6061 alloy with respect to recrystallisation.

2.4 Objectives of this work

Given the sparse and limited literature on the synthesis, characterisation and thermal response of UFG alloys in the Al–Mg–Si system, and especially the AA6061 alloy, in addition, given the lack of studies on the thermal response of these new UFG aluminium alloys considering the strict requirements for the possible application of these alloys in space which is $-210^{\circ}\text{C} \leq T \leq 150^{\circ}\text{C}$ for satellites and spacecrafts when in LEO conditions [72], the major objectives of this master thesis work are summarised as follows:

1. Obtain and characterise a CG AA6061 alloy using mainly DSC and TEM to revisit investigations on the precipitation sequence;
2. Synthesise an UFG AA6061 alloy from the CG AA6061 alloy using HPT;
3. Apply the characterisation methods within modern electron microscopy, such as scanning transmission electron microscopy (S/TEM), TEM and analytical elemental mapping through STEM-EDX in both CG and UFG AA6061 alloys as a function of the temperature peaks obtained from DSC;
4. Establish a comparative case study between both CG and UFG AA6061 alloys with respect to their inherent precipitation sequences considering the two different microstructural morphologies;
5. Investigate the thermal stability of the UFG AA6061 through *in situ* TEM heating methods; and
6. Evaluate the applicability of the UFG AA6061 alloy in the space environment in comparison with the new UFG AlMgZnCuAg crossover aluminium alloy synthesised and tested similarly by Willenshofer *et al.* in our research group [6, 16, 17].

3 Methodology

In this chapter, a short description of the experimental methods used in this work will be introduced. Then, the specific parameters and methodology applied using these methods to synthesise and characterise the obtained UFG AA6061 alloy will be given.

3.1 Description of the experimental methods

3.1.1 Arc/spark optical emission spectrometry

In recent decades, multiple analytical techniques have been employed to analyse the microstructure and chemical composition of pure metals and alloys. On the latter, the use of these techniques is aiming at performing analysis of major and trace element identification. Multiple sophisticated methods have been developed such as optical emission spectrometry (OES). Using this technique, the composition of elements in samples can be determined from either an inductively-induced plasma or a direct spark coupled with an optical spectrometer. This technique has been commercially available since 1974 and, due to its reliability, multi-elemental feature and high performance, it has become a widely used technique in both routine research and more specific analyses [73]. Arc/spark OES was used in this present work to measure the initial composition of the commercial CG AA6061 alloy.

3.1.2 Differential scanning calorimetry

Differential scanning calorimetry (DSC) is a well-established thermoanalytical method used to characterise thermodynamics and kinetics of phase transitions and precipitates in age-hardenable aluminium alloys. It works by measuring the difference in heat flux required to raise the temperature of a sample versus a reference material. The process involves heating the sample and reference material at a constant rate in a controlled environment. As the sample undergoes phase changes, such as melting or crystallisation, it absorbs (endothermic) or releases (exothermic) energy in the form of heat. This thermal energy is compared directly to known enthalpy changes of the reference material determined from previous experiments. In continuously heated DSC experiments, the heat flow between the sample and the reference is monitored over the temperature range of interest to elucidate the thermal behaviour of the sample [74].

During continuous DSC heating of aluminium and its alloys, precipitation (a solid-state phase transformation) triggers peaks in the heat flux thermogram. These peaks represent the amount of energy either released or absorbed during the precipitation process and can be directly proportional to the associated enthalpy change.

When precipitates begin to nucleate and grow, they release heat to their surroundings, causing them to heat up. This process is called exothermic because it gives off heat. On the other hand, when these precipitates dissolve, they absorb heat from their surroundings, cooling them. This process is called endothermic because it requires heat from the environment to dissolve. A typical DSC heat flux cell is shown in Figure 7 extracted from Lang *et al.* [74]. DSC was used in this work to investigate the precipitation sequence in both CG and UFG AA6061 alloys.

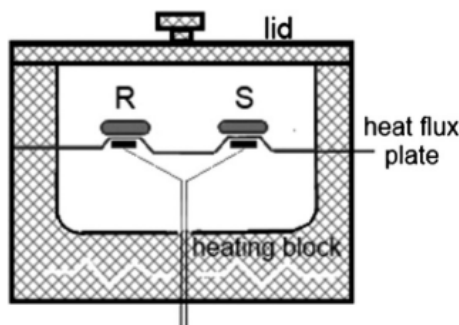


Figure 7: Schematic illustration of a DSC heat flux cell. The sample is denoted by S and the reference is denoted by R. Note: Reproduced from Lang *et al.* [74].

3.1.3 Transmission electron microscopy

TEM has gained immense popularity in materials science because it is well-suited for characterising the microstructure of diverse materials. In modern TEMs, the ability to carry out analytical measurements at both the nano- and atomic-scales is an important resource available for the modern metallurgist. A typical TEM is shown in Figure 8 reproduced from a book written by Fultz and Howe [75].

In a TEM, an electron beam is used to analyse a thin and electron-transparent sample (thicknesses ≤ 100 nm). First, electrons are produced using, for example, thermionic emission where a cathode made of a tungsten filament is heated up until electrons are emitted from the surface by overcoming the potential-energy barrier. In another way, electrons can be generated by field emission. In this latter method, a high negative potential is applied to an electrode by inducing a strong potential gradient on its surface, by this, electrons are emitted from the surface.

After emission, electrons are accelerated to an energy in the range of 60–300 keV. After the electron gun stage, the area of the specimen which is illuminated and the brightness are controlled using the condenser lens system and apertures. This objective lens aperture controls the illumination, resolution, depths of field and focus, the angular resolution of the diffraction pattern and the image contrast, in the case of the condenser aperture, it limits the size of the electron beam on the specimen which helps to control the illumination intensity on the specimen as well as to reduce spherical aberration effects. After the condenser system, the electrons are transmitted through a specimen and undergo into scattering. Those electrons scattered by the sample are

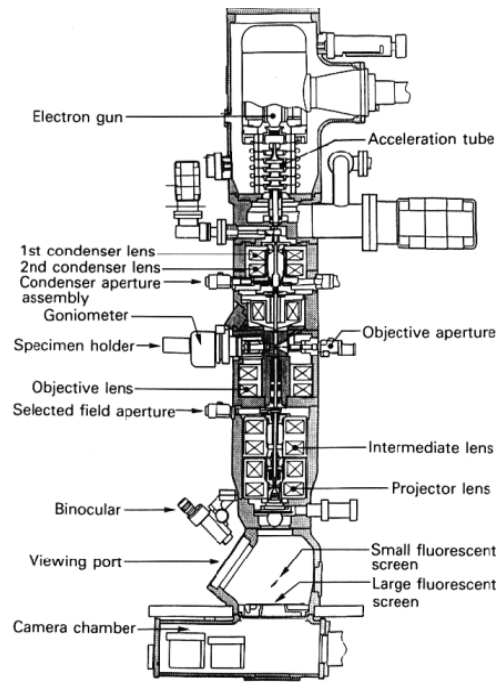


Figure 8: A cross-sectional profile of a common TEM. Note: Reproduced from Fultz and Howe [75].

focused by the objective lens and form a diffraction pattern (DP) in the back focal plane where the electrons scattered by the same angle are focused. Subsequently, electrons emanating from a single point on the sample are concentrated, producing an image on the designated image plane. This initial image can be magnified by successively employing intermediate and projection lenses [76].

BFTEM images are generated by scattered electrons using the objective aperture to let only the direct beam through. In contrast, dark-field (DFTEM) images are generated by obstructing the unscattered beam with a diaphragm, allowing one or more scattered diffracted beams to pass through the objective aperture. DFTEM micrographs are valuable for identifying planar defects, precipitates, and stacking faults [76]. Conventional TEM analysis was used in this work to characterise the microstructure of both CG and UFG AA6061 alloy and the corresponding DSC temperature peaks influence in the modification of these microstructures.

3.1.4 Scanning transmission electron microscopy

STEM is a mode of operation for a TEM and is particularly useful within the context of analytical characterisation. In this mode, a focused electron beam is used to scan and raster over the specimen. A typical STEM diagram is shown in Figure 9. After the specimen, a set of STEM detectors is inserted to capture the electrons transmitted during the raster. These are the high-angle annular dark-field (HAADF), low-angle annular dark-field (LAADF), and bright-field (BF) detectors. This configuration allows separate processing of the different signals obtained from the specimen [76].

If an EDX detector is utilised to capture the X-rays emitted during the scanning process of

the electron beam transmission across the specimen, it enables the generation of an elemental chemical map of the sample. STEM additionally possesses the capability to utilise incoherent elastic scattered electrons HAADF images. Commonly referred to as Z-contrast images, HAADF signals have the potential to offer high-resolution representations of atomic columns [76].

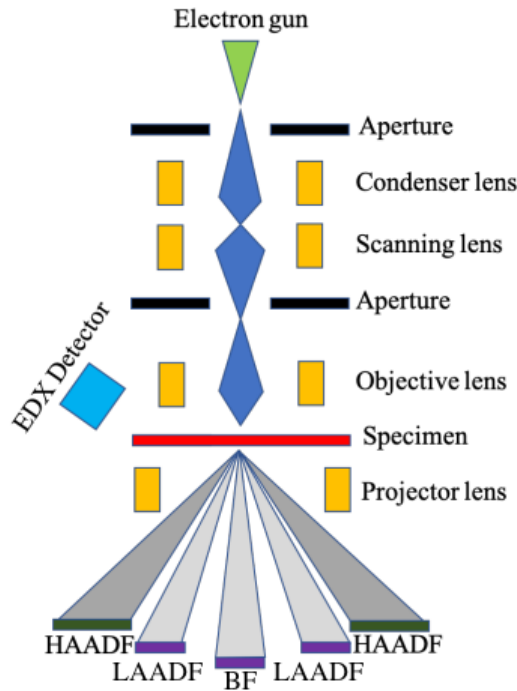


Figure 9: STEM mode within the TEM. Extracted from Tunes [76].

3.1.5 *In situ* TEM experiments

TEM is widely used as a dynamic research tool to study nano- and atomic-scale mechanism of complex material processes [77]. TEMs are also suitable for *in situ* experiments, where the dynamic response of a material subjected to an applied external stimulus can be observed, filmed, and recorded as it occurs in real-time inside the microscope [78].

All of this analysis can be performed at high visibility by employing *in situ* TEM sample holders, which can be regarded as “small laboratories” in the column of the microscope [78]. However, one of the main obstacles is the limited space available in the objective lens pole-piece for this device [77]. Recently, advances in the use of micro-electro-mechanical systems (MEMS), enable materials to be probed in the TEM in conditions that were not possible with previous instrumentations [79]. This innovative technology enables high-precision, electrical, thermal, and mechanical manipulation of individual nanostructures. At the same time, it facilitates real-time measurement of their properties, atomic resolution imaging, electron diffraction, and spectroscopy [77].

Such systems can as well help solve the problem of thermal drift and longer waiting times for system stabilisation when using *in situ* heating. With MEMS it is possible to cool and heat

quickly without reducing image quality or increasing wait times. Cooling rates can reach 1 millions of Kelvin per second, which is not achievable via any other metallurgical method [80]. *In situ* TEM heating experiments were performed in this work using a MEMS furnace holder to investigate the microstructural response of the UFG AA6061 alloy to heating.

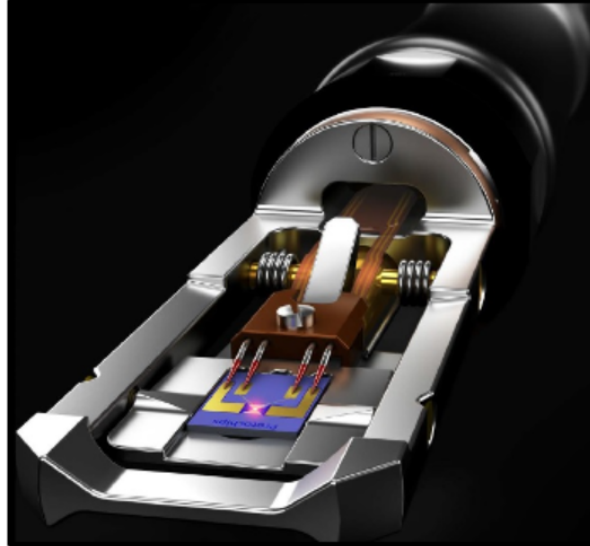


Figure 10: TEM holder with an E-chip used for heating experiments with *in situ* TEM. Note: Extracted from Protochips *apud* Coradini [81].

3.2 Synthesis and characterisation of the UFG AA6061 alloy

3.2.1 Preparation of the CG AA6061 alloy

The samples of the CG AA6061 were first cut, and then casted in a furnace Indutherm MC100V with ≈ 80 g in weight in a copper mould. The chemical composition was determined via arc/spark OES using an SpectroMaxX, and the results are reported in the table 3.1.

CG AA6061	Si	Mg	Cu	Mn	Fe	Cr	Zn	Ti
AA6061	0.767	0.857	0.230	0.128	0.425	0.206	0.071	0.038

Table 3.1: Experimental chemical composition of the commercial CG AA6061 alloy (wt%).

The obtained slabs were then homogenised with a heating ramp of $1^{\circ}\text{C}\cdot\text{min}^{-1}$ until it reached 580°C , and the slabs were held at this temperature for 8 hours. Subsequently, the slabs were cooled inside the oven with the door open for 4 hours. As the next step, the samples were processed by hot- and cold-rolling where their thicknesses were reduced from 12 mm to 1.5 mm as shown in Figure 11. Then, the CG AA6061 alloy was cut into smaller pieces for the DSC measurements. These smaller samples were solution heat-treated to 570°C for 20 minutes then quenched in water.



Figure 11: Final shape of the CG AA6061 alloy after homogenisation, hot- and cold-rolling prior HPT.

3.2.2 Synthesis of the UFG AA6061 alloy

For the production of the targeted UFG AA6061 alloy, as-cast slabs of the CG AA6061 alloy were used. Following procedures previously developed by Willenshofer *et al.* [6, 16, 17], HPT was carried out under a nominal hydrostatic pressure of 4 GPa for 10 revolutions at a rotational speed for 10 min per revolution, using a disk with 12 mm height and 30 mm diameter. The final shape of the obtained UFG AA6061 alloy is shown in Figure 12. The produced HPT disk is of ≈ 30 mm diameter and 7.5 mm of thickness. Due to processing conditions within the HPT set-up, there is a small core-shell in the sample after the HPT that is not used for the purposes of microstructural characterisation and analysis. This core-shell is around of 3 mm.



Figure 12: HPT equipment for synthesis of UFG AA6061 alloy and the final shape obtained after the HPT processing.

3.2.3 Thermal analysis

After synthesis of the UFG AA6061 alloy, DSC was carried out using a Netzsch DSC204 F1 Phönix. Nitrogen gas was used both as a purge and protective gas (each $20\text{ml}\cdot\text{min}^{-1}$). It is important to highlight that all thermal analysis experiments were performed at $10^\circ\text{C}\cdot\text{min}^{-1}$. For both the CG and UFG AA6061 alloy samples, the same measurements were carried out 3 times under similar and controlled parameters and initial conditions in order to ensure comparability of the data collected.

3.2.4 Electron-microscopy measurements

In parallel to DSC measurements, electron-microscopy characterisation with S/TEM was carried out using a Thermo Fisher Scientific Talos F200X electron microscope. For every exothermic peak obtained from the DSC measurements, samples of both CG and UFG AA6061 alloys were heated in a furnace Nabertherm N/15 with a heating ramp of $10^{\circ}\text{C}\cdot\text{min}^{-1}$ (identical to the DSC conditions) and then quenched in water. For every experiment, the quenched foils were thinned to $100\ \mu\text{m}$ by mechanical grinding/polishing, as shown in Figure 13, and then punched to circles of 3 mm diameter for TEM sample preparation.



Figure 13: Foils prepared with $100\ \mu\text{m}$ after mechanical polishing.

Prior S/TEM screening, the TEM samples were prepared by twin jet electro-polishing using a solution of 25 %vol. nitric acid and 75 %vol. methanol within the temperature range of -24°C to -30°C and a voltage of 13 V. For the TEM measurements, BFTEM, DFTEM, HAADF, LAADF, BF-STEM and SAED pattern measurement techniques were used. Elemental mapping with EDX was also performed.

3.2.5 *In situ* TEM thermal stability measurements

In situ TEM heating was carried out using the Talos F200X electron-microscope with a Protochips fusion select *in situ* heating/cooling holder with an uncoated MEMS e-chip. Sample preparation for *in situ* measurements was carried out according to literature [82] using a sample after electro-

polishing (as shown in Figure 14). The material was heat-treated within a TEM using a linear heating-rate of $10^{\circ}\text{C}\cdot\text{min}^{-1}$.



Figure 14: HPT sample used both for electron-microscopy investigations and *in situ* TEM heating experiments.

3.2.6 Grain size estimation

For grain size measurements in the case of CG AA6061 alloy, the sample was evaluated after solution heat treatment. It was prepared via metallography, using techniques such as mechanical grinding and polishing, and followed by electrochemically etched with Barker's reagent (1.8%vol. of Fluoridric acid in water) at 25 V for 60 seconds. Etched samples were subsequently analysed with polarised light by Optical Microscopy (OM). The images obtained were analysed using the program ImageJ [83] where the grain sizes were manually determined with length measurements. In the case of the UFG AA6061 alloy, the use of OM to estimate the grain sizes was not possible due to its limited spatial resolution. However for this UFG AA6061 alloy, grain size measurements considering width and length were manually performed using Velox software with micrographs acquired by S/TEM.

4 Results

The following section presents the results of the CG and UFG AA6061 alloys, with all the different techniques used.

4.1 The coarse grained AA6061 alloy

4.1.1 Grain size measurements

The CG AA6061 alloy after solution heat treatment exhibits an average grain size of $67.6 \pm 18.9 \mu\text{m}$, as shown in Figure 15. Grain size measurement is an useful indicator for comparing the sample conditions before and after the HPT process and also to assess the significant reduction in grain size from the micron to the nanometre scale, which is an objective of this study.

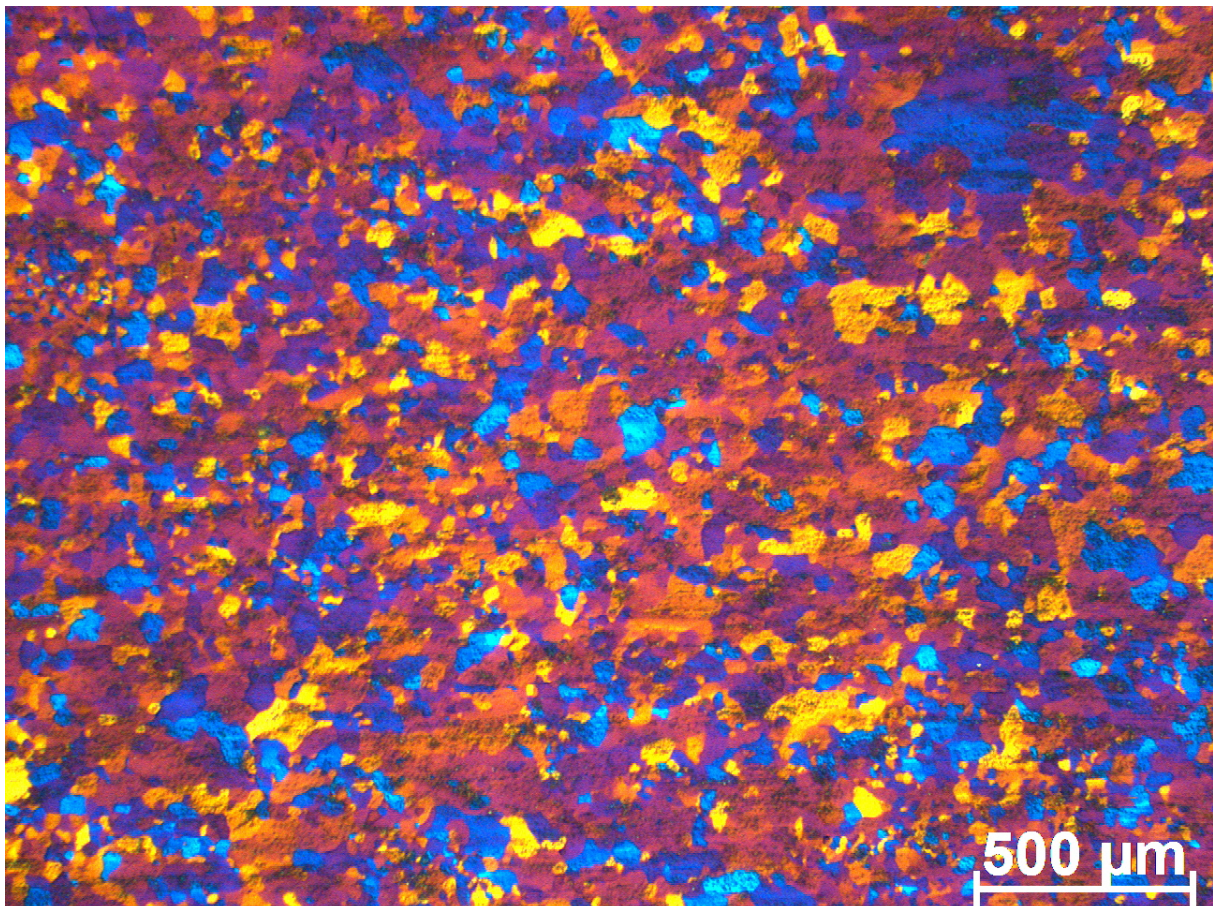


Figure 15: Microstructural morphology of the CG AA6061 alloy after processing. Micrograph was obtained through OM with polarised light after etching. Average grain size was $67.6 \pm 18.9 \mu\text{m}$.

4.1.2 Differential Scanning Calorimetry

The precipitation sequence of the CG AA6061 alloy was determined by DSC and it is shown as heat flow signals peaks in Figure 16. In Figure 16, four exothermic peaks at 88, 242, 298, and 477°C were identified. As discussed below in detail, the precipitation sequence of the CG AA6061 alloy shows similarities with the results of experiments carried out by other research groups [63, 67, 84].

The first peak at 88°C has been attributed to the formation of clusters of Si atoms, clusters of Mg atoms, co-clusters containing both Mg and Si atoms, and GP-I zones. At 242°C, formation of β'' is expected, while the peak at 298°C is associated with the formation of β' . The last peak at 477°C is related with the formation of stable β -phase or Mg_2Si [63, 67, 84]. In contrast to the findings of Dutta *et al.* [67] and Edwards *et al.* [63], we have not deconvoluted the second peak to reveal the possible overlap of GP-I, GP-II and β'' phases (see Figure 6) as our second peak in Figure 16 has not shown such a tendency for peak overlapping in the way that Dutta *et al.* observed [67].

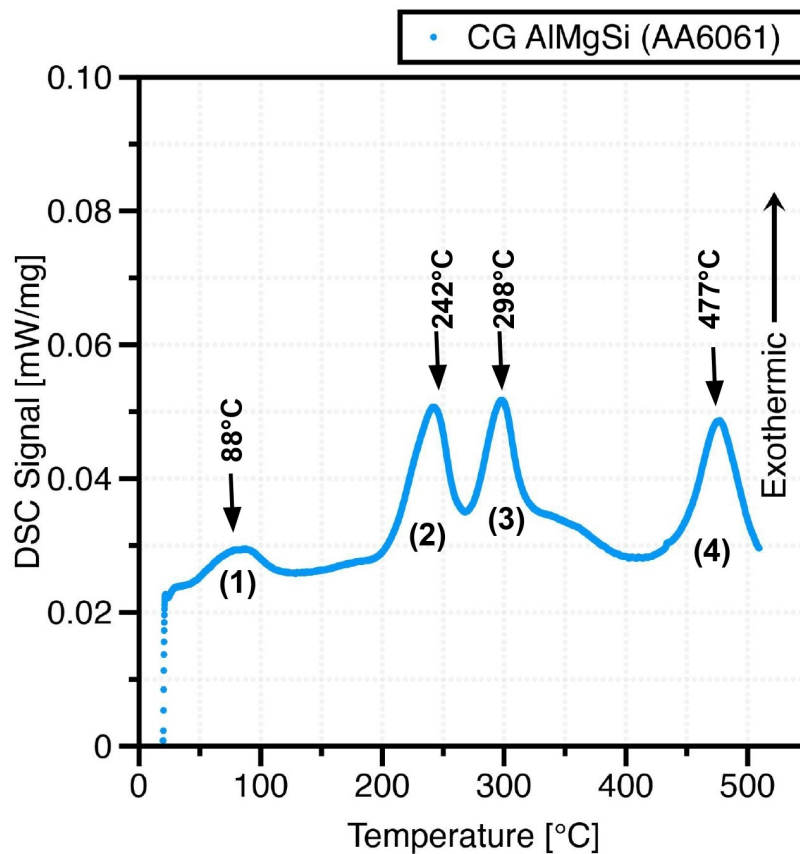


Figure 16: The thermogram obtained via DSC from the CG AA6061 alloy. These experiments were performed with a linear heating rate of $10^{\circ}\text{C}\cdot\text{min}^{-1}$.

4.1.3 Conventional and analytical scanning/transmission electron microscopy

S/TEM was performed to investigate the microstructure of the CG AA6061 alloy in each temperature peak detected in the DSC experiments, *i.e.*, each exothermic peak at 88, 242, 298, and 477°C. The results of the S/TEM investigations are shown in the set of micrographs obtained via BF-STEM, LAADF and SAED in Figure 17.

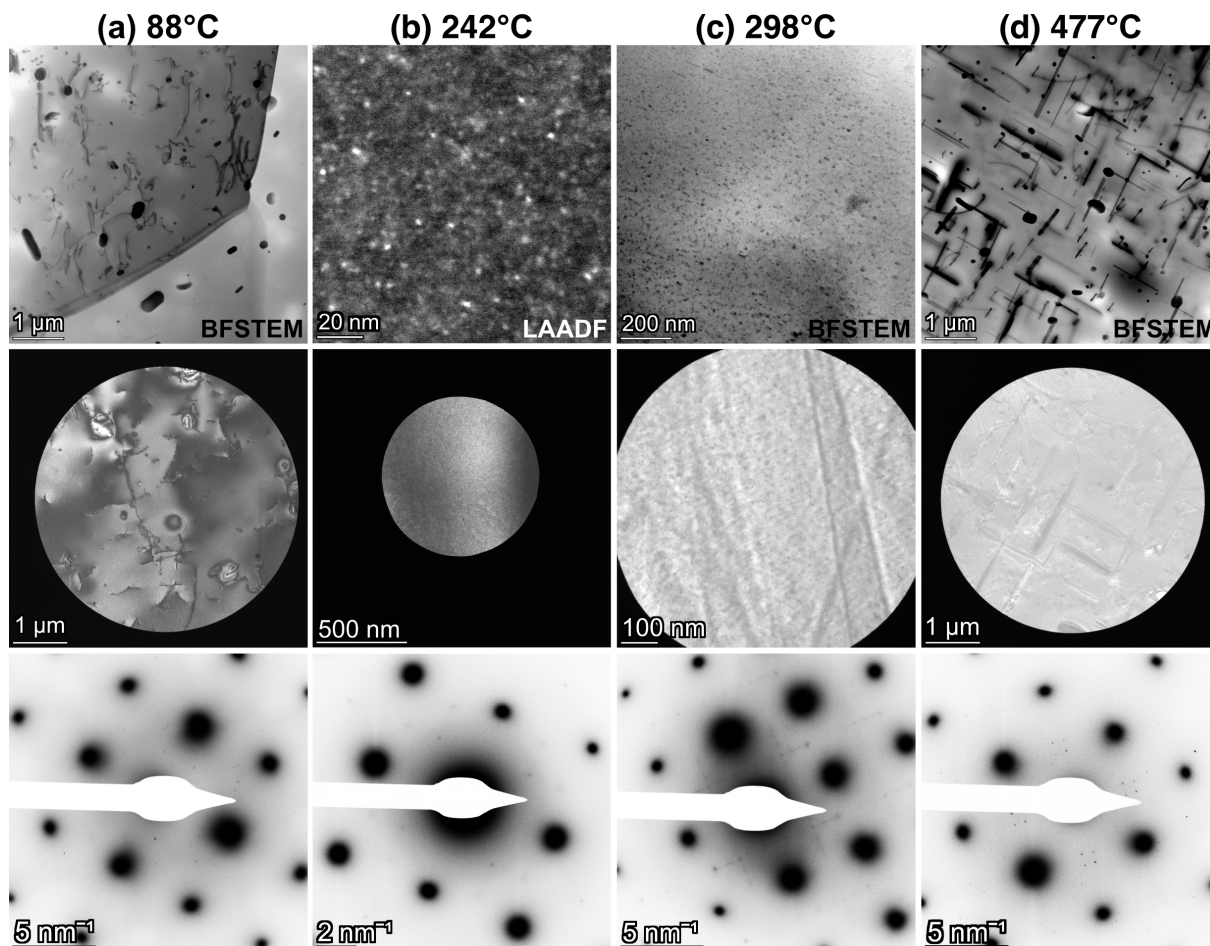


Figure 17: S/TEM micrographs and SAED patterns obtained from the CG AA6061 alloy at different temperatures according to the identified DSC peaks in Figure 16. Note: the SAED pattern had their colour inverted and both brightness and contrast were adjusted to better visualisation of the spots pertaining to the precipitates.

By analysing the results presented in Figure 17, one may notice that different contrast techniques and magnifications were used. This was intended to better visualise and/or assist to reveal the (possible) presence of clusters, GP zones, and precipitates. As noticeable in Figure 17(b) corresponding to the peak 242°C, due to the size, areal density and nature of the precipitates in this case, only the LAADF detector revealed differences in contrast between the matrix and the precipitates: here, the precipitates are round-white with respect to the matrix.

STEM-EDX mapping was carried out for the elemental and quantification analyses of the microstructure of the CG AA6061 alloy samples from same temperature peaks obtained via DSC. Figure 18 present these elemental maps for the major elements (Al, Mg, and Si) as a function of the

DSC-peak temperature. At 88°C, no precipitation was observed in the alloy, apart from Si crystals. Precipitation was noticeable at 242°C, as well as at 298 and 477°C, but differ in composition, size and morphology which will be discussed in the next chapter.

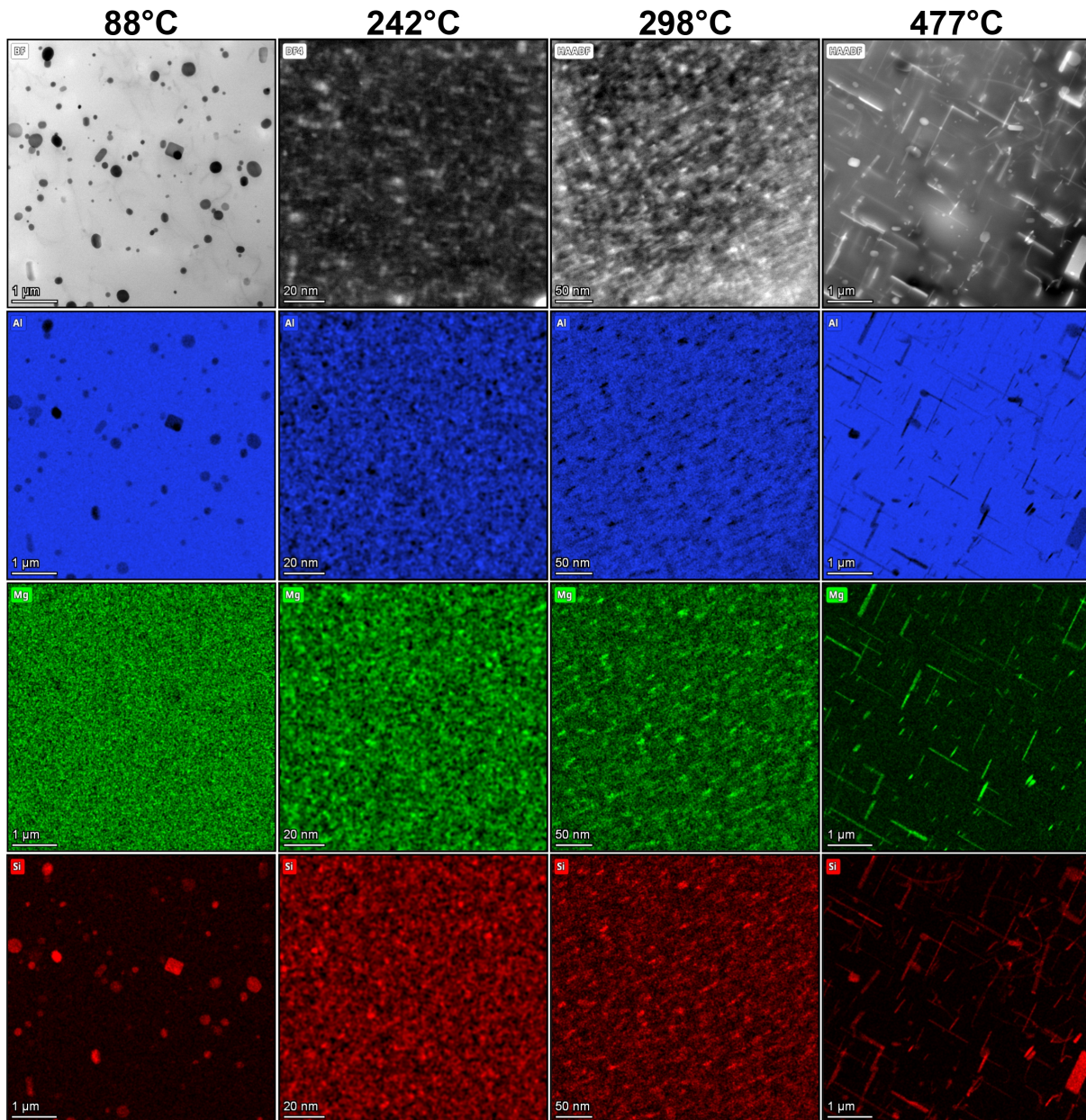


Figure 18: The STEM-EDX mapping of CG AA6061 alloy samples show the elemental maps of the major elements in the alloy at temperatures obtained from DSC results.

4.1.4 The estimation of the Mg/Si ratio

With the elemental maps obtained via the STEM-EDX technique, it was possible to both estimate the Mg/Si ratio and size of the precipitates in the temperature peaks where precipitation has been observed, *i.e.*, the temperature peaks at 242, 298, and 477°C (see Figure 18). In the 88°C case, no

hardening precipitates, or clusters or GP-zones were identified, apart from pure Si crystals which are not the focus of the work presented in this thesis, therefore, they were not quantified.

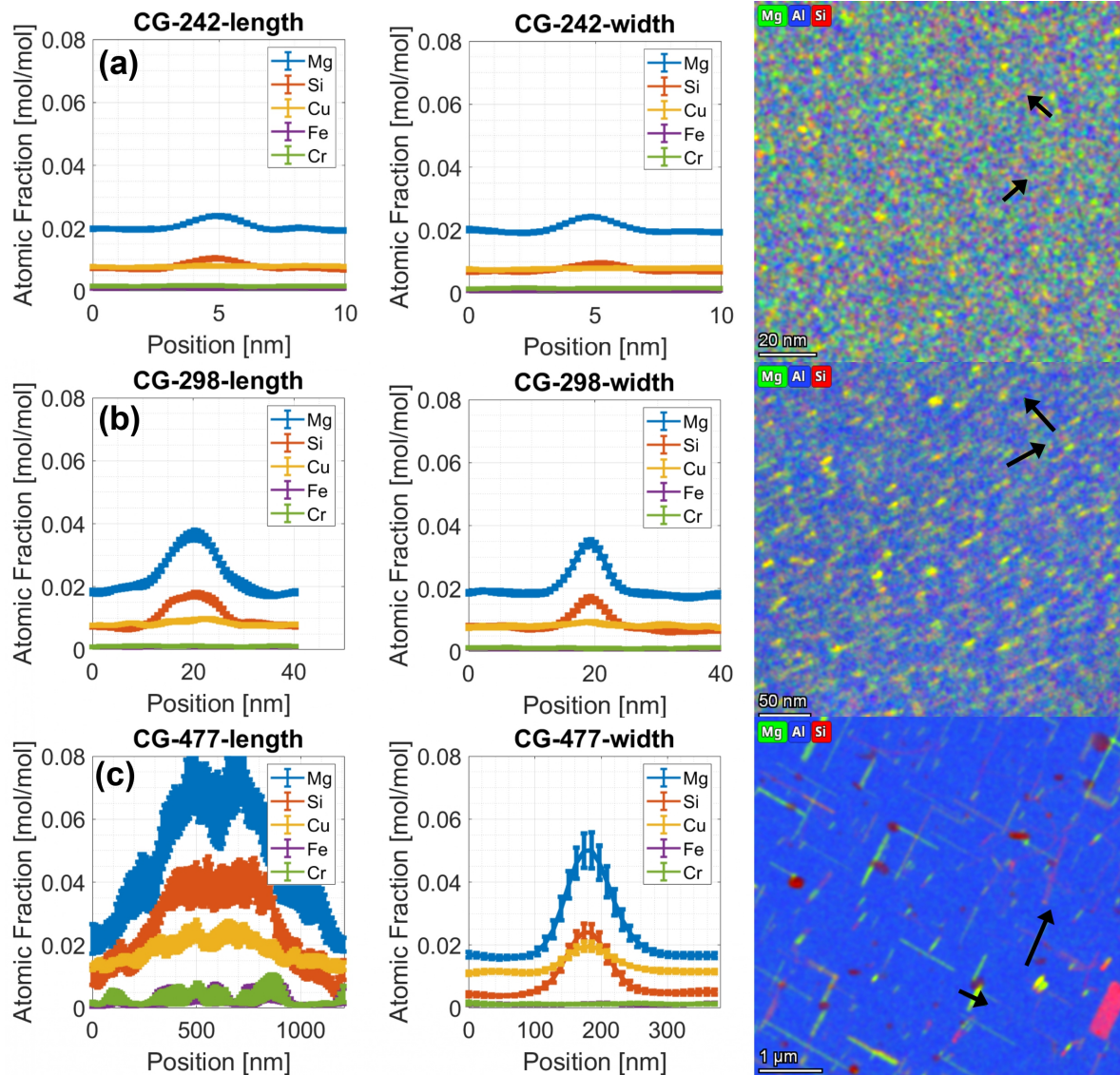


Figure 19: Mg/Si ratio (length and width) of precipitates presented in CG AA6061 alloy according to temperatures obtained via DSC results. Note: Around 20 precipitates were measured. Smaller precipitates may lead to overestimation of the content of both Mg and Si due to matrix effects.

Temperature Peak	242°C	298°C	477°C
Mg/Si ratio (length)	2.30 (3.60 nm)	2.09 (17.3 nm)	1.83 (1.05 μm)
Mg/Si ratio (width)	2.57 (3.57 nm)	2.06 (10.8 nm)	2.07 (162.1 μm)

Table 4.1: Mg/Si ratio and average size measurements of the precipitates identified in the CG AA6061 alloy.

The results of these estimation is presented in both Figure 19 and Table 4.1. With respect to the size of the precipitates, the measurements considered both width and length as the precipi-

tates, particularly in high-temperature, were observed to diverge from a spherical/rounded shape, which is the common case observed to low-temperature peaks.

4.2 The ultrafine-grained Al–Mg–Si alloy

4.2.1 Differential Scanning Calorimetry

The precipitation phenomenon in the UFG AA6061 alloy was investigated by DSC and it is shown as heat flow signals peaks in Figure 20. In contrast to the CG AA6061 alloy sample, which exhibited four exothermic peaks, the UFG AA6061 alloy sample showed only two exothermic peaks centred at both 225°C and 318°C.

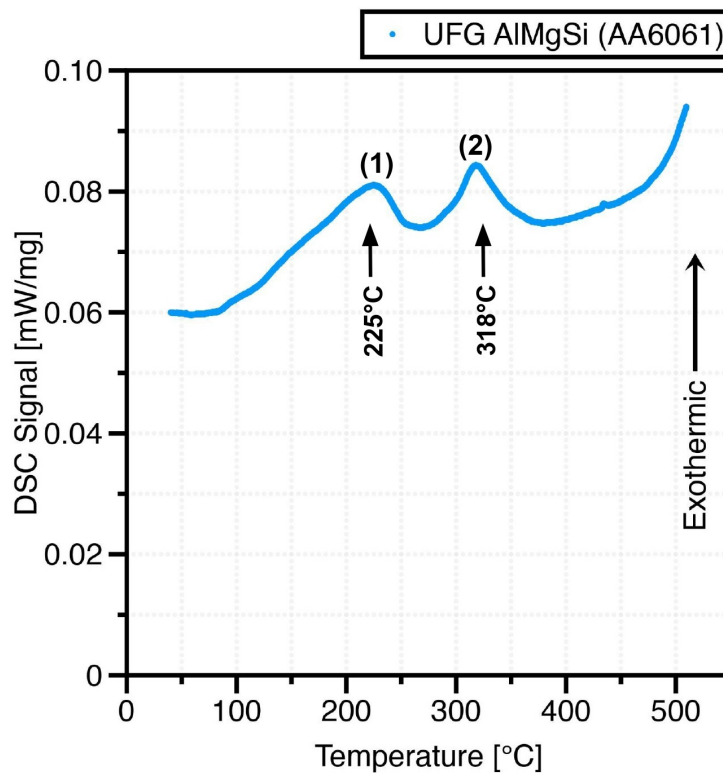


Figure 20: The thermogram obtained via DSC from the UFG AA6061 alloy. These experiments were performed with a linear heating rate of $10^{\circ}\text{C}\cdot\text{min}^{-1}$.

4.2.2 Conventional and analytical scanning/transmission electron microscopy

S/TEM was performed to investigate the microstructure of the UFG AA6061 alloy in each temperature peak detected in the DSC experiments, *i.e.*, each exothermic peak at 225°C and 318°C. In addition to this, one pristine sample (after HPT, but no heat-treatment) was evaluated. The results of the S/TEM investigations are shown in the set of micrographs obtained via BFSTEM and

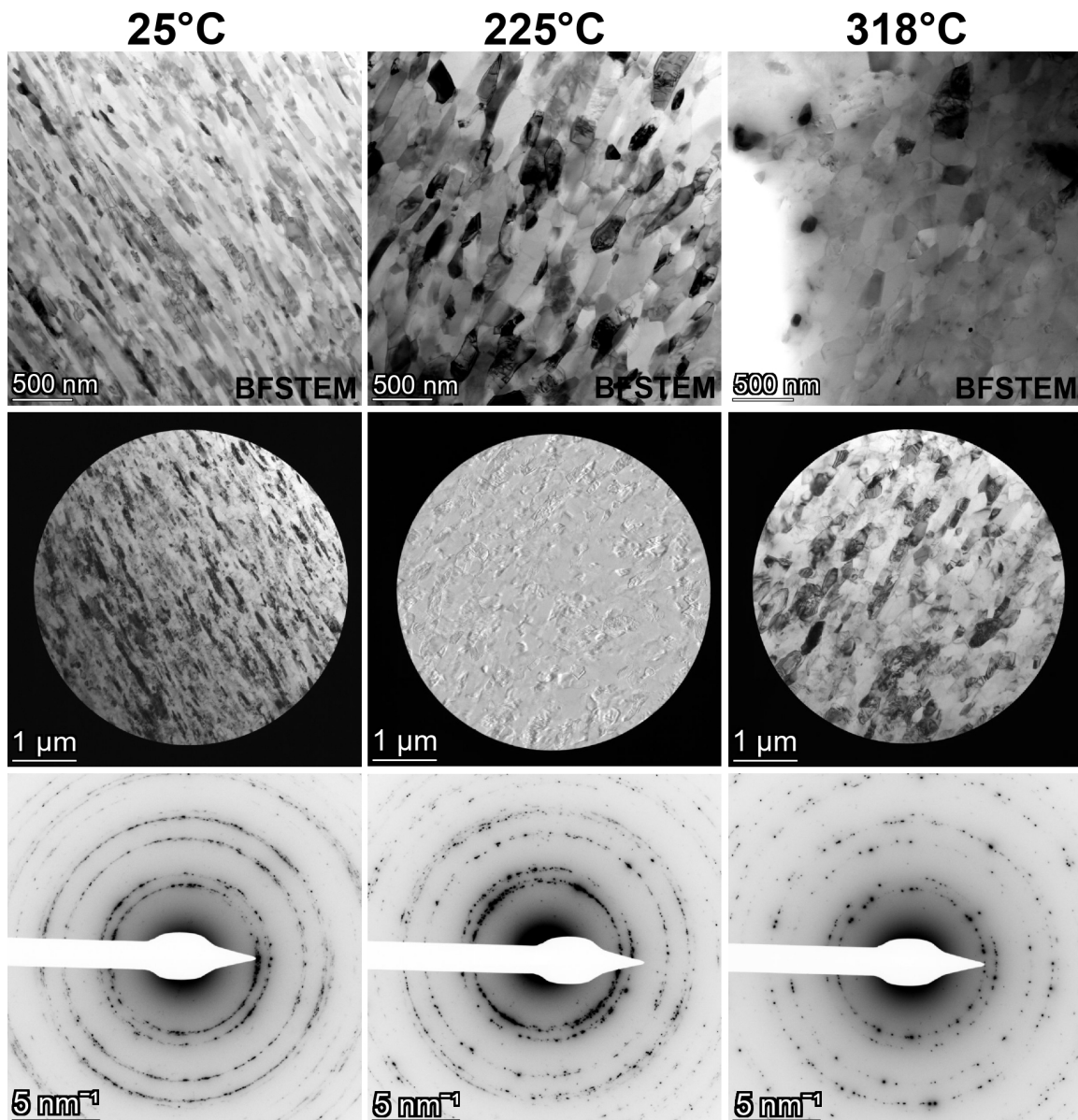


Figure 21: S/TEM micrographs and SAED patterns obtained from the UFG AA6061 alloy at room temperature and at 225°C and 318°C according to the identified DSC peaks in Figure 20.

SAED in Figure 21. All micrographs were captured at the same magnification to allow a consistent comparison of the effect of temperature on the grain size of the material.

STEM-EDX mapping was carried out for the elemental and quantification analyses of the microstructure of the UFG AA6061 alloy samples from same temperature peaks obtained via DSC, and in addition, one pristine sample was analysed. These elemental maps for the major elements (Al, Mg, and Si) are presented in Figure 22. Although at 25°C, no precipitation is observed, at both 225°C and 318°C, precipitates were observed in the UFG AA6061 alloy microstructure. In the first case, 225°C, precipitates were primarily observed at intra-granular position. These precipitates have grown at 318°C, but are still present mainly in the intra-granular positions, although some precipitates are trans-granular.

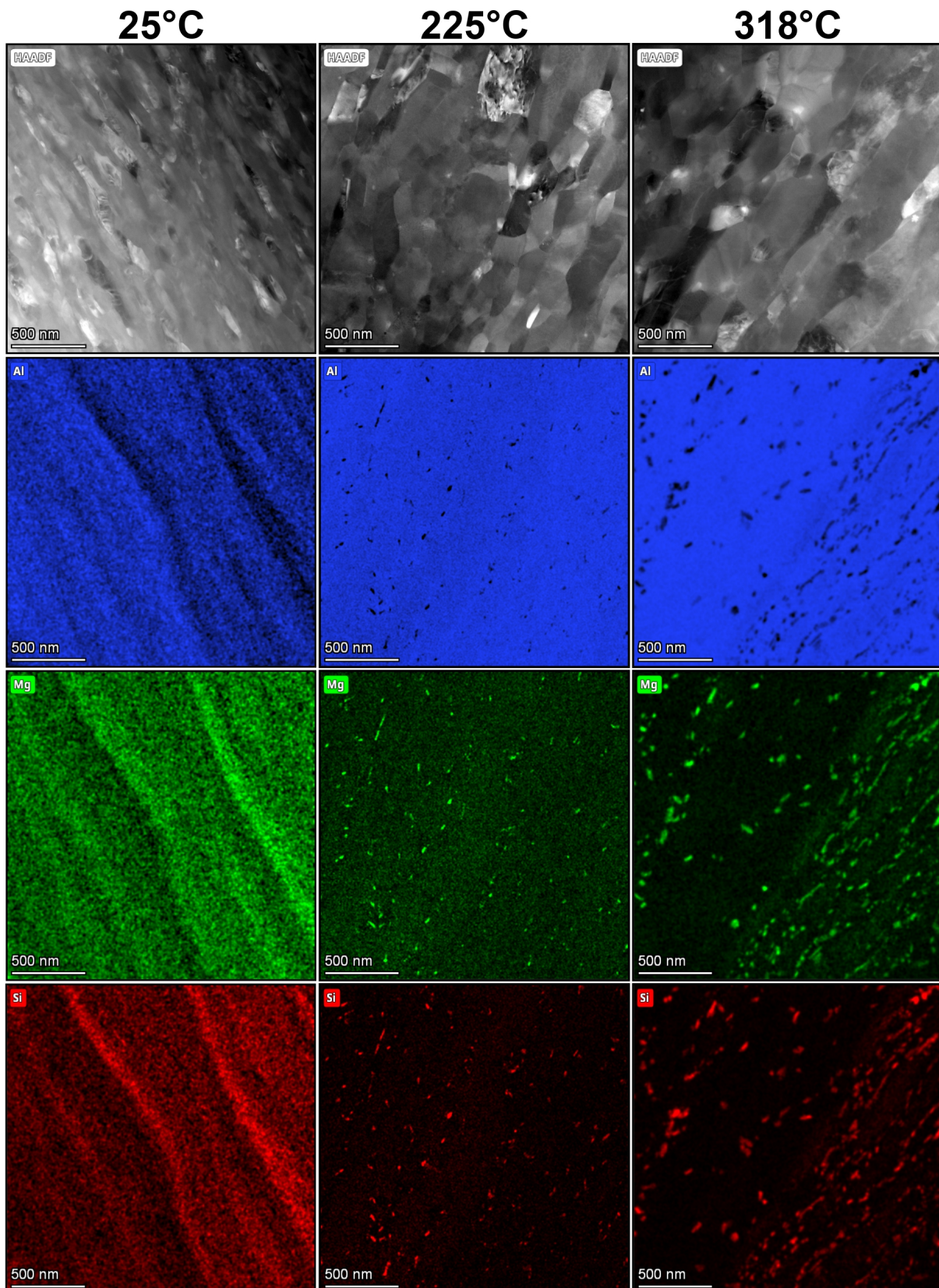


Figure 22: The STEM-EDX mapping of UFG AA6061 alloy samples show the elemental maps of the major elements in the alloy at room temperature, 225°C and 318°C according to the peaks obtained via DSC.

4.2.3 The estimation of the Mg/Si ratio

With the elemental maps obtained via the STEM-EDX technique, it was possible to both estimate the Mg/Si ratio and size of the precipitates in the temperature peaks where precipitation has been observed, *i.e.*, the temperature peaks at 225 and 318°C (see Figure 22).

The results of this estimation are presented in both Figure 23 and Table 4.2. With respect to the size of the precipitates, the measurements were made considering them spherical. As previously mentioned, in the sample evaluated at the as-received condition no hardening precipitates, or clusters or GP-zones were identified.

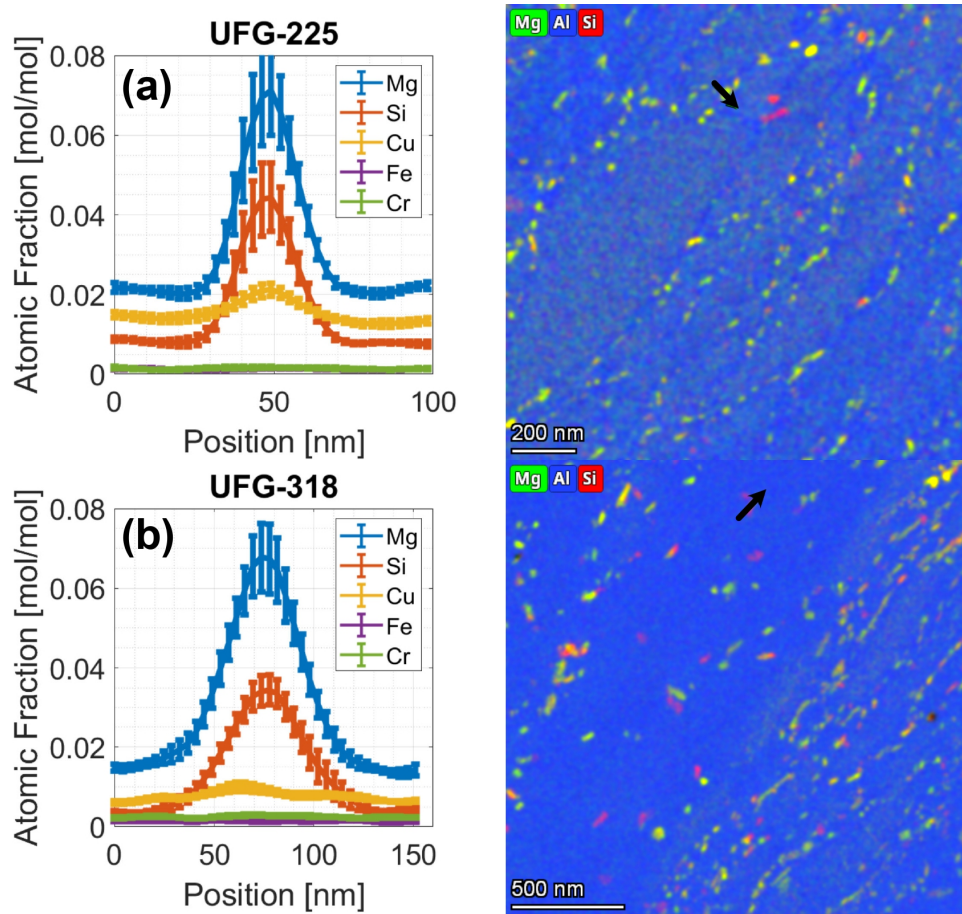


Figure 23: Mg/Si ratio (radius) of precipitates detected in the UFG AA6061 alloy according to temperatures obtained via DSC results. Note: Around 20 precipitates were measured. Smaller precipitates may lead to overestimation of the content of both Mg and Si due to matrix effects.

Temperature Peak	225°C	318°C
Mg/Si ratio (Radius)	1.60 (43.3nm)	1.96 (73.5nm)

Table 4.2: Mg/Si ratio and average size measurements of the precipitates identified in the UFG AA6061 alloy.

4.2.4 Grain size measurements

The grain size measurements for the UFG AA6061 alloy after both HPT and heat treatment at the three different temperatures (the temperature-peaks identified in DSC measurements) are shown in Figure 24.

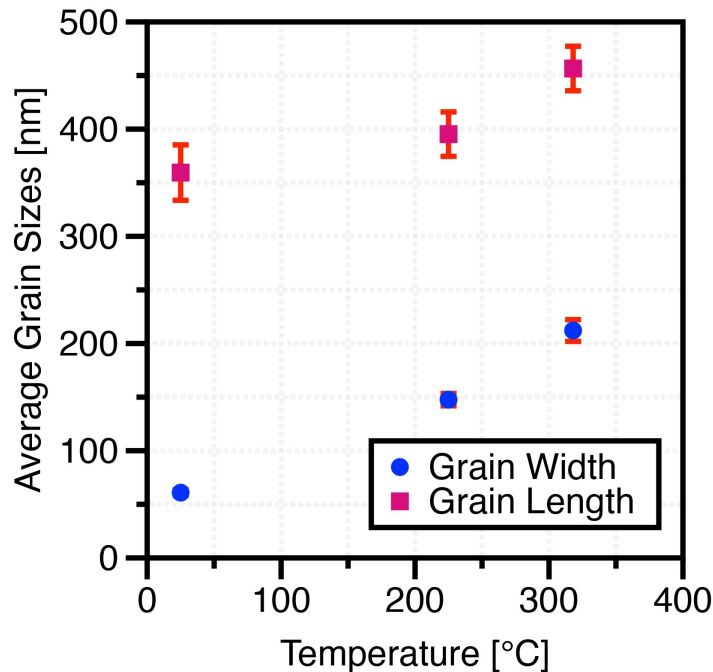


Figure 24: Grain size measurements (length and width) for the UFG AA6061 alloy at room temperature and at 225°C and 318°C.

The sample after HPT that was not thermally treated exhibited an average grain length of 359 ± 25 nm and a width of 61 ± 3 nm. For the sample treated at 225°C, the average grain length and width increased to 395 ± 21 nm and 148 ± 6 nm, respectively, and for the heat-treated at 318°C, these values further increased to 457 ± 21 nm in length and 212 ± 10 nm in width. These results indicate that the grain size gradually increases as a function of temperature as shown in Figure 24, but the width grows at a faster rate than the length, *i.e.*, from room-temperature to 318°C, the width increases 350% whereas the length increases 127%.

4.2.5 *In situ* TEM heating

In situ TEM heating experiments were performed on the UFG AA6061 alloy to investigate its thermal stability by monitoring grain growth and/or recrystallisation as a function of increasing temperature in realtime. At the same time, these experiments allowed the analysis of the growth and dissolution of Mg- and Si-rich precipitates. The evolution of the UFG AA6061 alloy according to the temperature ramp under *in situ* TEM conditions is presented in Figure 25.

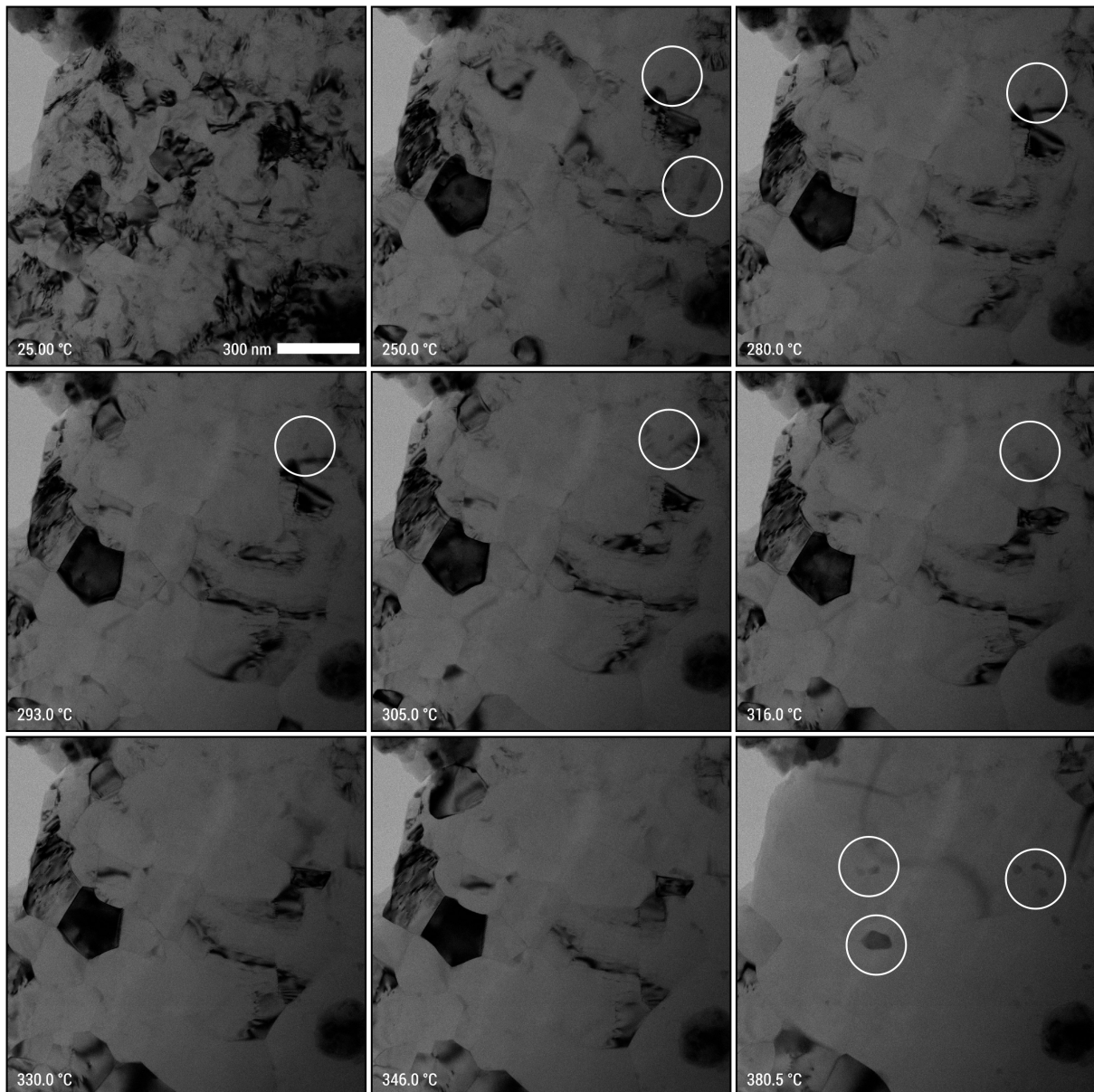


Figure 25: BFTEM micrographs showing *in situ* TEM experiments conducted as a function of temperature on the UFG AA6061 alloy. Note: Limited precipitation is observed at 250°C, as indicated by the white circles in micrographs, and in which dissolution started at around 316°C.

5 Discussion

5.1 Comparison CG vs UFG alloy

Differences between the CG AA6061 and the UFG AA6061 alloys were observed which are discussed below.

5.1.1 Coarse grained alloy

The combination of S/TEM and DSC results introduced by Figures 16 and 17 indicates that the precipitation sequence of the CG AA6061 alloy present differences with respect to the temperature.

At 88°C in S/TEM revealed neither hardening phases nor clusters in the alloy matrix. Si crystals were observed in the EDX mapping in Figure 18 which are related with primary phases nucleation during casting. This sample was also analysed at higher magnifications and in the same way no further precipitates were found. However, these early stages of precipitation were extensively studied by Dutta *et al.*, Edwards *et al.*, and Muyarama *et al.* [63, 67, 85], as mentioned by these authors, the hardening phases are related to the formation of clusters of Si atoms, clusters of Mg atoms, co-clusters containing both Mg and Si atoms, and GP-I zones, which takes place at this temperature, but are not detectable by electron-microscopy methods, but rather by atom probe tomography (APT) techniques [62]. The corresponding SAED pattern taken at 88°C corroborates that these clusters were not detectable by electron-microscopy. The detection of these clusters was only ascribed in our work only by the presence of an exothermic peak in the DSC presented in Figure 16, which agrees with previous APT data reviewed by Dumitraschkewitz *et al.* [62].

Regarding the analysis of the second peak at 242°C, there is a discrepancy with the conclusions of previous authors. The analysis of Dutta *et al.* [67] identified two overlapping peaks near 240°C, which required a deconvolution process as illustrated in Figure 6. These two overlapping peaks were also found in Edwards *et al.* study [63]. In contrast, the DSC analysis of our study (see Figure 16) revealed a single peak at 242°C without any indications of overlapping peaks (*e.g.*, “bumps” in the peak profile). By using the LAADF-STEM detector, we identified nanometre-sized precipitates in the 242°C sample. This detector allows the identification of the strain posed by these precipitates, which is higher than the matrix, then allowing their detection. Such a technique has recently been introduced by Marioara *et al.* [86]. The corresponding SAED pattern exhibits superlattice faint spots, corroborating the precipitates are present and are semi-coherent with the matrix. These results agree with the electron-diffraction analysis for β'' performed by Dutta *et al.*, which is shown in Figure 6: in our case, our SAED pattern represents an overlap between the SAED patterns of the two deconvolved peaks by Dutta *et al.* [67]. Additionally, the SAED patterns are similar to those previously reported by Edwards *et al.* [63] and Yassar *et al.* [84]. This indicates

that the DSC peak number two corresponds to the formation of ordered needle-shaped GP-II zones or β'' phases. The STEM-EDX mapping in Figure 18 shows these precipitates enriched in Mg and Si. The Mg/Si ratio was estimated, to the best of our knowledge for the first time considering their geometrical dimensions, *i.e.*, we have estimated this ratio with respect to the compositional measurements along the length and the width. At 242°C, the β'' precipitates have an average length of 3.60 nm with a Mg/Si ratio in length of 2.30 as well an average width of 3.57 nm with a Mg/Si ratio in width of 2.57. Due to the lack of higher precision spatial quantification techniques at the time, Andersen *et al.* [87] reported in the past that the Mg/Si ratio of β'' precipitates should be either less or equal to 1 or higher or equal than 1. Our results, provide therefore, a better understanding on the Mg/Si ratio of these β'' precipitates.

In samples treated up to the peak of 298°C, S/TEM revealed homogeneous distribution of precipitates with rod-shape and bigger than the precipitates found in the 242°C peak sample. This allowed direct detection with BFSTEM (Figure 17(c)). In addition, the SAED pattern shows the presence of superlattice reflections which are attributed to these rod-shape precipitates. These results agree with previous DSC/TEM study by Dutta *et al.* [67] as is illustrated in Figure 6 peak c. This indicates that these rod-shape precipitates correspond to β' phase. Mg and Si were found to compose these precipitates in the EDX mapping presented in Figure 18. For these β' precipitates, we estimate an average length of 17.3 nm with a Mg/Si ratio in length of 2.09 as well as an average width of 10.8 nm with a Mg/Si ratio in width of 2.06. With respect to the β' precipitate sizes, our results are in agreement with both Andersen *et al.* [87] and Vissers *et al.* [88], who report these precipitates should be from 10 to 20 nm, although these authors report on diameter and not rods' length and width. With respect to the Mg/Si ratio for the β' precipitate, Andersen *et al.* [87] and Vissers *et al.* [88] report on ≈ 1.7 and 1.69, respectively. Our Mg/Si ratio is in between 2.06–2.09, slightly higher than Andersen *et al.* [87] and Vissers *et al.* [88]. This is due to the fact that the EDX technology has evolved from 1998 and 2007 (the dates of Andersen's and Visser's papers) to present days: it is well known that modern EDX detectors, like ours, present better energy resolution and higher throughput data collection (increasing the number of counts of X-rays) allowing a more precise identification of Mg/Si ratios for such small precipitates.

At 477°C, the stable β is expected [67]. Plate/needle-like precipitates can be observed in the microstructure of the CG AA6061 alloy at this temperature and they are significantly larger than the 242°C and 298°C cases. SAED patterns also shows the presence of micrometre-sized precipitates. Mg/Si ratio was 1.83 and 2.07 for both length and width, respectively. These values are closely aligned with Andersen *et al.* [87] who reported Mg/Si= equals 2 for Mg₂Si precipitates. Andersen also indicates a size of "microns" for this precipitates, other authors like Vissers *et al.* [88] indicates a size around 10-20 μm . Our analysis resulted in 1 and 162 μm in length and width respectively. The EDX mapping revealed the presence of Mg and Si in these β particles (as shown in Figure 18). In this case, pure Si particles were also observed in the mapping which corroborates that the alloy in this state has reached equilibrium [62]. These results are also consistent with previous research of Yassar *et al.* [84] that found β and Si precipitates at temperatures around

400°C with similar morphology, this same plate-like shape morphology was found by Fang *et al.* [89] in Al-Mg-Si aged samples.

5.1.2 Ultra-fine grained alloy

The combination of S/TEM and DSC results introduced by Figures 20 and 21 show the evolution of the UFG AA6061 alloy as a function of temperature and will be herein analysed and discussed in depth.

We have not detected the formation of GP zones in the UFG AA6061 alloy due to both the absence of DSC peaks below 225°C and absence of contrast and diffraction signal in the S/TEM. As precipitation is a diffusion-dependent phase transformation that takes place differently varying the alloy morphology, *i.e.*, grain sizes, such a difference in the precipitation sequence between the CG and UFG A6061 alloys has been attributed to accelerated diffusion and enhanced precipitation kinetics in UFG materials [17, 70]. The abundant number of grain boundaries in UFG materials provide rapid solid-state diffusion pathways to solutes, leading to altered precipitation behaviour when compared with CG materials. Consequently, this can reduce the critical size for GP-zone/precipitation formation, and therefore, may promote the early transformation of the β'' phase into β' or β phases [70].

Moreover, the peaks associated with precipitation in the DSC results presented in Figure 16 are shifted to lower temperatures: the first CG peak at 242°C is now at 225°C and the fourth CG peak at 477°C is now at 318°C. Now, we shall determine the precipitate sizes and Mg/Si ratio at these both peaks when in the UFG condition.

A sample was examined in the as-processed via HPT to evaluate the grain morphology and elemental distribution after SPD. For this case, no precipitation was observed in the S/TEM micrographs and SAED patterns (Figure 21), nor using STEM-EDX as shown in Figure 22. As HPT was performed at room temperature, dynamic precipitation was not observed in this sample in contrast to Sha *et al.* [70]: this is simply due to the fact that in our HPT procedure, no temperature was applied to facilitate SPD. Grain size measurements exhibited an average grain length of 359 ± 25 nm and a width of 61 ± 3 nm. These results are similar to the ones obtained by Willenshofer *et al.* [16] in the UFG aluminium crossover alloy that exhibits an average grain length of 294.3 ± 109.8 nm and a width of 91.4 ± 36.6 respectively. Measurements using the S/TEM micrographs reveal the diminished grain size in the UFG AA6061 alloy, which is also evident in the SAED pattern, showing the presence of Debye-Scherrer rings instead of monopattern/monograin in the case of the CG AA6061 alloy (see Figure 17).

In the first peak at 225°C, although the SAED pattern indicates the presence of nanometre-sized precipitates, the spots related with them are fainter and present a reduced signal when compared with the matrix due the fact that these precipitates are of a smaller volumetric density than the precipitates in the CG AA6061 alloy. The absence of high-intensity and clearer diffraction rings attributed to precipitation, impedes their identification via diffraction indexing. This can be

also attested in the STEM-EDX mapping in Figure 22 where the predominantly Mg-Si intra-granular disc-shaped precipitates are visible. It is important to compare that the areal density of precipitates in the UFG alloy at 225°C is significantly smaller when compared with the precipitates in the CG alloy at 242°C (compare the Mg/Si maps in both Figures 18 and 22). The estimated Mg/Si ratio of these precipitates is equal to 1.6, which according to previous research by Andersen *et al.* [87] indicates the formation of β' .

In the second peak at 318°C, the SAED patterns also revealed the presence of nanometre-sized precipitates. The reduced number of spots in this SAED pattern, compared to that observed at 225°C, and given that the diameters of the selected zones were equal, indicates the presence of larger grains at 318°C when compared with the 225°C. This is also in agreement with previous observations by Mohamed *et al.* [68]. The STEM-EDX mapping in Figure 22 shows predominantly rounded-shape precipitates, larger than the ones at 225°C. Additionally, it can be observed that the intra-granular (inside the grain boundaries) precipitation evolved into (partially) trans-granular (across the grains) precipitation. The Mg/Si ratio of these precipitates is equal to 1.96, which according to Andersen's previous research *et al.* [87] indicates the formation of the equilibrium phase β (Mg_2Si).

5.1.3 Remarks on the differences between the heat-treated CG and UFG AA6061 alloys

From the analysis of both CG and UFG AA6061 alloys with S/TEM and DSC, it is clear that the phenomenon of precipitation hardening is highly dependent on the average grain sizes of the alloys. As precipitation is of paramount importance for mechanical strength of alloys to be applied in space, we can conclude that in the UFG regime, the Al-Mg-Si presents limited precipitation ability. This is reflected by the fact that in the UFG AA6061 alloy, precipitation is mainly taking place within the intra-granular positions and in low volumetric densities when compared with the CG AA6061 alloy. In addition, we have observed that the phenomenon of precipitation is accelerated in the UFG alloy when compared with the CG counterpart. This is also reflected by the fact that intermediate metastable phases such as the β'' at not at all observed in the UFG AA6061 alloy, and that the equilibrium phase, the β or Mg_2Si , rapidly forms at smaller temperatures than in the CG alloy. Although precipitation is observed to be limited in the UFG AA6061 alloy, the fact the precipitation is mainly observed at grain boundaries, *i.e.*, intra-granular positions, poses the following questions:

1. Will this UFG AA6061 alloy with precipitation prone to take place along the grain boundaries recrystallise at lower or higher temperatures than the previously reported UFG pure aluminium and UFG AlMg alloy which was 200°C [54, 90]?
2. Will this UFG AA6061 alloy recrystallise at a lower or higher temperature than the record at around 300°C currently pertained to the UFG aluminium crossover alloy (AlMgZnCuAg)

reported by Willenshofer *et al.* [16]?

5.2 *In situ* thermal stability of the UFG AA6061 alloy

To answer the questions above, we resort to the application of the *in situ* TEM heating technique, where the microstructure of the UFG AA6061 alloy can be observed in real-time as a function of the temperature in an S/TEM. These results were shown in Figure 25,

The UFG AA6061 alloy microstructure started to exhibit recrystallisation around 180°C. Such recrystallisation accelerated when the temperature reached around 250°C. Interestingly, during the *in situ* TEM heating experiments, we have not detected smaller and nanometre-sized precipitates nucleating and growing in the alloy matrix. Therefore, we can conclude that the UFG AA6061 alloy is not stable at temperatures higher than 150-180°C, which would be a major requirement for space materials considering, for example, the thermal cycles a material can be subjected when in LEO conditions.

Limited precipitation of Mg₂Si phase can be observed in the white circles in Figure 25. The presence of larger Mg₂Si which appear to have formed through the process of Ostwald ripening [91], which involves the dissolution and subsequent re-precipitation of smaller clusters or precipitates that were not detectable under the studied conditions.

The fact that the precipitation of the Mg₂Si phase is observed to be limited in the UFG AA6061 alloy points to an interesting observation previously made by Tunes *et al.* [2] and Willenshofer *et al.* [6, 16]: considering a temperature ramp, the first set of authors reported that the β phase fraction is smaller than the T-phase fraction, the latter the hardening precipitate within the aluminium crossover alloy system of Al–Mg–Zn; the last set of authors calculated the enthalpy of formation of different hardening phases in multiple aluminium alloy systems, including the Al–Mg–Si and the Al–Mg–Zn. They concluded that T-phase presents an enthalpy of formation which is three order of magnitude smaller than conventional hardening phases in aluminium alloys, including the β phase. Lower enthalpy of formation and higher phase fractions indicate that T-phase precipitation is significantly accelerated in a UFG aluminium alloy when compared with the herein studied UFG AA6061 alloy. Acceleration means here that the precipitates will readily form intra-, trans- and inter-granular positions, acting as obstacles for grain boundary movement, thus preventing recrystallisation. This explains why the UFG AlMgZnCuAg aluminium crossover alloy retains the record temperature at which recrystallisation takes place in any UFG aluminium alloy.

In summary, the main difference between the T-phase in UFG aluminium crossover alloys and the β -phase in UFG AA6061 alloy within the same temperature range (25-400°C) is: (a) T-phase with higher volumetric density compared with the β -precipitates and (b) lower enthalpy of formation of T-phase precipitation when compared with β -phase precipitates. This implies that (a) T-phase restricts grain boundary movement and delays recrystallisation via intra-granular (along

grain boundaries) precipitation and growth and that (b) the T-phase is easily formed and extends through the microstructure by consuming the energy released by defects, dislocations, and grain boundaries of the UFG microstructure during heating.

6 Conclusions

This study explored the feasibility to synthesize and investigated the thermal stability of an UFG AA6061 alloy intended for applications in space. The development of ultrafine grains is crucial for enhancing the recombination and absorption of defects generated under conditions such as energetic particle irradiation, including solar proton exposure from the Sun as well as galactic cosmic rays and thermal cycling when in LEO conditions. For that, a stable UFG microstructure should feature hardening precipitates that are able to hinder grain boundary movement, preventing recrystallisation at elevated temperatures.

For that, we have obtained and characterised a CG AA6061 alloy using mainly DSC and TEM and we have revisited the precipitation sequence studies providing better quantification of Mg/Si elemental ratio as well as refined precipitation-size measurements when compared with previous literature on the topic [63, 67, 87, 88].

With the obtained as-cast slabs of the CG AA6061 alloy, we successfully synthesised a UFG AA6061 alloy via the application of the SPD principle through HPT.

By applying the characterisation methods such as S/TEM, STEM-EDX mapping, and DSC, we have observed that the precipitation kinetics differ between CG and UFG AA6061 alloys. The UFG alloy achieves the equilibrium β -phase in a more accelerated way and at lower temperatures compared to the CG alloy. This difference is most likely due to the accelerated diffusion rates at the grain boundaries of the UFG alloy, as previously investigated by Willenshofer *et al.* [16]. With that, we have also established a comparative case study between both the CG and UFG AA6061 alloys in terms of precipitation morphology and sizes as well as chemical constituency. We provide, to the best of our knowledge, a characterisation matching DSC peaks and S/TEM for the UFG AA6061 alloy system, and for first-time considering the application STEM-EDX mapping technique and Mg/Si ratio estimation.

Considering the development and application UFG aluminium alloys in extreme environments, this study emphasizes the critical importance of delaying the temperature at which recrystallization processes take place. This work indicated that such a task was already accomplished in the Al–Mg–Zn–Cu–Ag system (UFG crossover alloy, previously demonstrated and studied by Willenshofer *et al.* [16]), but not in the Al–Mg–Si (the commercial and widely used AA6061) due to the low temperature for recrystallisation obtained via *in situ* TEM heating experiments herein reported: we show that the UFG AA6061 alloy experiences thermal instabilities at temperatures as low as 150°C and that at 250°C, the recrystallisation is already at a point where the initial UFG structure is lost.

We therefore recommend – for field UFG aluminium alloys considering their thermal stability for space applications – that microstructural control takes place when the hardening phase of an aluminium alloy system exhibits both (i) a highly negative enthalpy of formation, leading to ac-

celerated precipitation nucleation and growth kinetics even considering an alloy matrix composed of ultrafine grains, and (ii) a large volumetric density for the phase nucleation and grow, allowing precipitates to be formed extensively at intra- and trans-granular positions. Such a phase does not exist in the Al–Mg–Si, but it exists in the Al–Mg–Zn–Cu–Ag system, and it is known as T-phase [6, 16, 17].

Bibliography

1. Lewis, J. A. *Space exploration in a changing international environment* (Rowman & Littlefield, 2014) (cit. on p. 4)
2. Tunes, M. A. *et al.* Prototypic Lightweight Alloy Design for Stellar-Radiation Environments. *Advanced science* **7**, 2002397 (2020) (cit. on pp. 4, 5, 6, 7, 8, 9, 10, 11, 45)
3. Mouritz, A. P. *Introduction to aerospace materials* (Elsevier, 2012) (cit. on pp. 4, 7, 8)
4. Finckenor, M. M. *Materials for spacecraft tech. rep.* (American Institute of Aeronautics and Astronautics, 2018) (cit. on pp. 4, 7)
5. Ghidini, T. Materials for space exploration and settlement. *Nature materials* **17**, 846–850 (2018) (cit. on pp. 4, 7)
6. Willenshofer, P. D. *et al.* Radiation-resistant aluminium alloy for space missions in the extreme environment of the solar system 2022. arXiv: 2210.03397 [cond-mat.mtrl-sci]. <https://arxiv.org/abs/2210.03397> (cit. on pp. 4, 5, 6, 7, 9, 11, 14, 21, 27, 45, 48)
7. Moldwin, M. *An introduction to space weather* (Cambridge University Press, 2022) (cit. on pp. 5, 7)
8. Lohmann, W. *et al.* Microstructure and mechanical properties of medium energy (600-800 MeV) proton irradiated commercial aluminium alloys. *Radiation effects* **101**, 283–299 (1987) (cit. on pp. 5, 9, 10)
9. Singh, B. N. *et al.* Microstructural changes in commercial aluminum alloys caused by irradiation with 800-MeV protons in *Radiation-Induced Changes in Microstructure: 13th International Symposium (Part I)* (1987) (cit. on pp. 5, 9)
10. Abd El-Hameed, A. M. & Abdel-Aziz, Y. Aluminium Alloys in Space Applications: A Short Report. *Journal of Advanced Research in Applied Sciences and Engineering Technology* **22**, 1–7 (2021) (cit. on pp. 5, 6, 8, 9, 14, 15)
11. Greaves, G. *et al.* Enhanced sputtering yields from single-ion impacts on gold nanorods. *Physical review letters* **111**, 065504 (2013) (cit. on p. 5)

12. Glynn, P. C. & Moser, T. L. *Orbiter structural design and verification in Space Shuttle Technical Conference, part 1* (ed Chaffee, N.) (NASA, 06/1983), 345–356 (cit. on p. 5)
13. Stemper, L. *et al.* On the potential of aluminum crossover alloys. *Progress in Materials Science* **124**, 100873 (2022) (cit. on p. 5)
14. Stemper, L. *et al.* Age-hardening response of AlMgZn alloys with Cu and Ag additions. *Acta Materialia* **195**, 541–554 (2020) (cit. on p. 5)
15. Stemper, L. *et al.* Giant hardening response in AlMgZn (Cu) alloys. *Acta Materialia* **206**, 116617 (2021) (cit. on p. 5)
16. Willenshofer, P. *et al.* Precipitation behaviour in AlMgZnCuAg crossover alloy with coarse and ultrafine grains. *Materials Research Letters* **11**, 1063–1072 (2023) (cit. on pp. 6, 12, 14, 15, 21, 27, 43, 45, 47, 48)
17. Willenshofer, P. *et al.* Comparative analysis of experimental techniques for microstructural characterization of novel nanostructured aluminium alloys. *Materials Characterization*, 114154 (2024) (cit. on pp. 6, 14, 21, 27, 43, 48)
18. Zhang, X. *et al.* Radiation damage in nanostructured materials. *Progress in Materials Science* **96**, 217–321 (2018) (cit. on pp. 6, 11)
19. Brailsford, A. D., Bullough, R. & Hayns, M. R. Point defect sink strengths and void-swelling. *Journal of Nuclear Materials* **60**, 246–256 (3 1976) (cit. on p. 6)
20. Bullough, R., Hayns, M. & Wood, M. Sink strengths for thin film surfaces and grain boundaries. *Journal of Nuclear Materials* **90**, 44–59. ISSN: 00223115 (1-3 05/1980) (cit. on p. 6)
21. Shkuratov, Y. G. *et al.* A twofold mission to the moon: Objectives and payloads. *Acta Astronautica* **154**, 214–226 (2019) (cit. on p. 7)
22. Valentin, J. *et al.* *The 2007 recommendations of the international commission on radiological protection 2-4* (Elsevier Oxford, 2007) (cit. on p. 7)
23. Tunes, M. A., De Oliveira, C. & Schön, C. G. Multi-objective optimization of a compact pressurized water nuclear reactor computational model for biological shielding design using innovative materials. *Nuclear engineering and design* **313**, 20–28 (2017) (cit. on p. 7)

24. Kawai, N. *et al.* Single microparticle launching method using two-stage light-gas gun for simulating hypervelocity impacts of micrometeoroids and space debris. *Review of Scientific Instruments* **81** (2010) (cit. on p. 8)
25. Rajan, R. *et al.* TRENDS IN ALUMINIUM ALLOY DEVELOPMENT AND THEIR JOINING METHODS. *Reviews on Advanced Materials Science* **44** (2016) (cit. on p. 8)
26. Bouzekova-Penkova, A. & Miteva, A. Some aerospace applications of 7075 (B95) aluminium alloy. *Aerospace Research in Bulgaria* **34**, 165–179 (2022) (cit. on p. 8)
27. Czajkowski, C. *Response of structural materials to radiation environments* tech. rep. (Brookhaven National Lab.(BNL), Upton, NY (United States), 1997) (cit. on p. 9)
28. Kolluri, M. Neutron Irradiation Effects in 5xxx and 6xxx Series Aluminum Alloys: A Literature Review. *Radiat. Eff. Mater* (2016) (cit. on p. 9)
29. Böning, K. & Von Der Hardt, P. Physics and safety of advanced research reactors. *Nuclear Instruments and Methods in Physics Research Section A: Accelerators, Spectrometers, Detectors and Associated Equipment* **260**, 239–246 (1987) (cit. on p. 9)
30. Hajewska, E. Investigation of the properties of aluminium alloys used in the construction of nuclear research reactors (1993) (cit. on p. 9)
31. Vogl, G. & Weiss, B. Der Einfluss von neutronenbestrahlung auf die ausscheidungskinetik iv einer übersättigten Al-Cu-Legierung. *Acta Metallurgica* **13**, 578–582 (1965) (cit. on p. 9)
32. Katz, L., Herman, H. & Damask, A. Precipitation in neutron-irradiated Al-base Cu. *Acta Metallurgica* **16**, 939–945 (1968) (cit. on p. 9)
33. Ghauri, I. & Afzal, N. Effects of neutron irradiation on the stress relaxation rate in Al–Cu–Mg alloy. *Journal of Physics D: Applied Physics* **40**, 6044 (2007) (cit. on p. 9)
34. Liu, K. *et al.* Structural changes in age-hardenable aluminium alloys induced by low temperature neutron irradiation. *Radiation Effects* **15**, 37–49 (1972) (cit. on p. 9)
35. Farrell, K. Microstructure and tensile properties of heavily irradiated 5052-0 aluminum alloy. *Journal of Nuclear Materials* **97**, 33–43 (1981) (cit. on p. 9)

36. Piatti, G., Fiorini, P. & Schiller, P. High purity aluminium alloys for experimental fusion reactors. *Nuclear Engineering and Design. Fusion* **1**, 137–158 (1984) (cit. on p. 9)
37. Ismail, Z. Effect of low dose neutron irradiation on the mechanical properties of an AlMgSi alloy. *Radiation Effects and Defects in Solids* **112**, 105–110 (1990) (cit. on p. 9)
38. Was, G. S. & Was, G. S. Irradiation hardening and deformation. *Fundamentals of Radiation Materials Science: Metals and Alloys*, 669–733 (2017) (cit. on p. 11)
39. Markushev, M. *et al.* Structure and properties of ultra-fine grained aluminium alloys produced by severe plastic deformation. *Materials Science and Engineering: A* **234**, 927–931 (1997) (cit. on pp. 11, 13)
40. Langdon, T. G. *Processing of aluminium alloys by severe plastic deformation* in *Materials science forum* **519** (2006), 45–54 (cit. on pp. 11, 13)
41. Leo, P. *et al.* Properties and deformation behaviour of severe plastic deformed aluminium alloys. *Journal of Materials Processing Technology* **182**, 207–214 (2007) (cit. on pp. 11, 13)
42. Sabirov, I., Murashkin, M. Y. & Valiev, R. Nanostructured aluminium alloys produced by severe plastic deformation: New horizons in development. *Materials science and engineering: A* **560**, 1–24 (2013) (cit. on pp. 11, 13)
43. Kumar, H. *et al.* Severe plastic deformation: A state of art. *Materials Today: Proceedings* (2023) (cit. on pp. 11, 12, 13, 14)
44. Valiev, R. The new trends in fabrication of bulk nanostructured materials by SPD processing. *Journal of materials science* **42**, 1483–1490 (2007) (cit. on p. 12)
45. Hall, E. The deformation and ageing of mild steel: III discussion of results. *Proceedings of the Physical Society. Section B* **64**, 747 (1951) (cit. on p. 12)
46. Petch, N. J. The cleavage strength of polycrystals. *J. Iron Steel Inst.* **174**, 25–28 (1953) (cit. on p. 12)
47. Das, B., Dixit, U. S. & Panda, B. N. in *Advances in Forming, Machining and Automation: Select Proceedings of AIMTDR 2021* 47–59 (Springer, 2022) (cit. on pp. 12, 13)

48. Nuphairode, C. K. *et al.* The evolvement of mechanical properties and microstructure of commercial aluminum alloy 6061 via high-pressure torsion. *Jurnal Kejuruteraan* **32**, 531–538 (2020) (cit. on p. 13)
49. Murashkin, M. *et al.* Fatigue behavior of an ultrafine-grained Al-Mg-Si alloy processed by high-pressure torsion. *Metals* **5**, 578–590 (2015) (cit. on p. 13)
50. Khamei, A. *et al.* Hot and cold tensile behavior of Al 6061 produced by equal channel angular pressing and subsequent cold rolling. *Iranian Journal of Materials Forming* **2**, 30–42 (2015) (cit. on p. 13)
51. Verleysen, P. & Lanjewar, H. Dynamic high pressure torsion: A novel technique for dynamic severe plastic deformation. *Journal of Materials Processing Technology* **276**, 116393 (2020) (cit. on p. 13)
52. Zhilyaev, A. P. & Langdon, T. G. Using high-pressure torsion for metal processing: Fundamentals and applications. *Progress in Materials science* **53**, 893–979 (2008) (cit. on p. 13)
53. Nurislamova, G. *et al.* Nanostructure and related mechanical properties of an Al–Mg–Si alloy processed by severe plastic deformation. *Philosophical Magazine Letters* **88**, 459–466 (2008) (cit. on p. 13)
54. Valiev, R. Z. & Langdon, T. G. Principles of equal-channel angular pressing as a processing tool for grain refinement. *Progress in materials science* **51**, 881–981 (2006) (cit. on pp. 14, 44)
55. Abd El-Aal, M. I. The influence of ECAP and HPT processing on the microstructure evolution, mechanical properties and tribology characteristics of an Al6061 alloy. *Journal of Materials Research and Technology* **9**, 12525–12546 (2020) (cit. on p. 14)
56. Ogunsemi, B. *et al.* A review of various improvement strategies for joint quality of AA 6061-T6 friction stir weldments. *Journal of Materials Research and Technology* **11**, 1061–1089 (2021) (cit. on p. 14)
57. Aster, P. *et al.* Unraveling the potential of Cu addition and cluster hardening in Al-Mg-Si alloys. *Materialia*, 102188 (2024) (cit. on pp. 15, 16)
58. Baruah, M. & Borah, A. Processing and precipitation strengthening of 6xxx series aluminium alloys: A review. *Int. J. Mater. Sci* **1**, 40–48 (2020) (cit. on pp. 16, 17, 18)

59. Sathaiah, S. & Acharyya, S. G. *Effect of homogenization cooling on the precipitation behavior of 6061 Al alloy in AIP Conference Proceedings* **1832** (2017) (cit. on p. 16)
60. Pogatscher, S. *et al.* Mechanisms controlling the artificial aging of Al–Mg–Si Alloys. *Acta Materialia* **59**, 3352–3363 (2011) (cit. on pp. 16, 17, 18)
61. Rambabu, P. *et al.* Aluminium alloys for aerospace applications. *Aerospace Materials and Material Technologies: Volume 1: Aerospace Materials*, 29–52 (2017) (cit. on pp. 16, 17, 18)
62. Dumitraschkewitz, P. *et al.* Clustering in age-hardenable aluminum alloys. *Advanced Engineering Materials* **20**, 1800255 (2018) (cit. on pp. 17, 18, 41, 42)
63. Edwards, G. *et al.* The precipitation sequence in Al–Mg–Si alloys. *Acta materialia* **46**, 3893–3904 (1998) (cit. on pp. 17, 18, 19, 31, 41, 47)
64. Martinsen, F. A. *et al.* Reversal of the negative natural aging effect in Al–Mg–Si alloys. *Acta materialia* **60**, 6091–6101 (2012) (cit. on pp. 17, 18)
65. Derlet, P. *et al.* A first-principles study of the β'' -phase in Al–Mg–Si alloys. *Journal of Physics: Condensed Matter* **14**, 4011 (2002) (cit. on p. 18)
66. Yan, L. *et al.* Pre-aging on early-age behavior and bake hardening response of an Al-0.90 Mg-0.80 Si-0.64 Zn-0.23 Cu alloy. *Progress in Natural Science: Materials International* **26**, 398–403 (2016) (cit. on p. 18)
67. Dutta, I. & Allen, S. A calorimetric study of precipitation in commercial aluminium alloy 6061. *Journal of materials science letters* **10**, 323–326 (1991) (cit. on pp. 18, 19, 31, 41, 42, 47)
68. Mohamed, I. F. *et al.* Aging behavior of Al 6061 alloy processed by high-pressure torsion and subsequent aging. *Metallurgical and Materials Transactions A* **46**, 2664–2673 (2015) (cit. on pp. 20, 44)
69. Roven, H. J., Liu, M. & Werenskiold, J. C. Dynamic precipitation during severe plastic deformation of an Al–Mg–Si aluminium alloy. *Materials Science and Engineering: A* **483**, 54–58 (2008) (cit. on p. 20)
70. Sha, G. *et al.* Strength, grain refinement and solute nanostructures of an Al–Mg–Si alloy (AA6060) processed by high-pressure torsion. *Acta Materialia* **63**, 169–179 (2014) (cit. on pp. 20, 43)

71. Singh, D., Jayaganthan, R., *et al.* Effect of post cryorolling treatments on microstructural and mechanical behaviour of ultrafine grained Al–Mg–Si alloy. *Journal of Materials Science & Technology* **30**, 998–1005 (2014) (cit. on p. 21)
72. Iyengar, V. K. C. *Modelling of the thermal environment and subsystem for a 6U cubesat in GTO orbit* PhD thesis (Luleå University of Technology, Space Technology, 2020) (cit. on p. 21)
73. Seidel, P. *et al.* Comparison of elemental analysis techniques for the characterization of commercial alloys. *Metals* **11**, 736 (2021) (cit. on p. 22)
74. Lang, P. *et al.* Thermo-kinetic prediction of metastable and stable phase precipitation in Al–Zn–Mg series aluminium alloys during non-isothermal DSC analysis. *Journal of Alloys and Compounds* **609**, 129–136 (2014) (cit. on pp. 22, 23)
75. Fultz, B. & Howe, J. M. *Transmission electron microscopy and diffractometry of materials* (Springer Science & Business Media, 2012) (cit. on pp. 23, 24)
76. Tunes, M. A. *Transmission electron microscopy study of radiation damage in potential nuclear materials* PhD thesis (University of Huddersfield, 2020) (cit. on pp. 24, 25)
77. Zhang, M. *et al.* In situ transmission electron microscopy studies enabled by microelectromechanical system technology. *Journal of materials research* **20**, 1802–1807 (2005) (cit. on p. 25)
78. Ferreira, P., Mitsuishi, K. & Stach, E. In situ transmission electron microscopy. *Mrs Bulletin* **33**, 83–90 (2008) (cit. on p. 25)
79. Tunes, M. A. *et al.* A contamination-free electron-transparent metallic sample preparation method for MEMS experiments with in situ S/TEM. *arXiv preprint arXiv:2012.02941* (2020) (cit. on p. 25)
80. Dumitraschkewitz, P. *et al.* MEMS-Based in situ electron-microscopy investigation of rapid solidification and heat treatment on eutectic Al–Cu. *Acta Materialia* **239**, 118225 (2022) (cit. on p. 26)
81. Santa Rosa Coradini, D. *Nanometallurgy of nonferrous metals* English. no embargo. PhD thesis (Montanuniversität Leoben (000), 2023) (cit. on p. 26)

82. Tunes, M. A. *et al.* A fast and implantation-free sample production method for large scale electron-transparent metallic samples destined for MEMS-based in situ S/TEM experiments. *Materials* **14**, 1085 (2021) (cit. on p. 28)
83. Schneider, C. A., Rasband, W. S. & Eliceiri, K. W. NIH Image to ImageJ: 25 years of image analysis. *Nature methods* **9**, 671–675 (2012) (cit. on p. 29)
84. Yassar, R. S., Field, D. P. & Weiland, H. Transmission electron microscopy and differential scanning calorimetry studies on the precipitation sequence in an Al–Mg–Si alloy: AA6022. *Journal of materials research* **20**, 2705–2711 (2005) (cit. on pp. 31, 41, 42)
85. Murayama, M. & Hono, K. Pre-precipitate clusters and precipitation processes in Al–Mg–Si alloys. *Acta materialia* **47**, 1537–1548 (1999) (cit. on p. 41)
86. Marioara, C. D. *et al.* Atomic structure of clusters and GP-zones in an Al-Mg-Si alloy. *Acta Materialia* **269**, 119811 (2024) (cit. on p. 41)
87. Andersen, S. *et al.* The crystal structure of the β'' phase in Al–Mg–Si alloys. *Acta Materialia* **46**, 3283–3298 (1998) (cit. on pp. 42, 44, 47)
88. Vissers, R. *et al.* The crystal structure of the β' phase in Al–Mg–Si alloys. *Acta Materialia* **55**, 3815–3823 (2007) (cit. on pp. 42, 47)
89. Fang, X. *et al.* Precipitation sequence of an aged Al-Mg-Si alloy. *Journal of Mining and Metallurgy, Section B: Metallurgy* **46**, 171–180 (2010) (cit. on p. 43)
90. Valiev, R. Z., Islamgaliev, R. K. & Alexandrov, I. V. Bulk nanostructured materials from severe plastic deformation. *Progress in materials science* **45**, 103–189 (2000) (cit. on p. 44)
91. Voorhees, P. W. The theory of Ostwald ripening. *Journal of Statistical Physics* **38**, 231–252 (1985) (cit. on p. 45)

Appendix

Table 6.1: List of artificial intelligence used in this thesis.

Objective	Part of AI (in %)	Tool / Version	Remark	Reference to prompting
Improvement of linguistic readability	0	Chat GPT v4.0	n/a	-